

Vertical velocity in the interaction between inertia-gravity waves and submesoscale baroclinic vortical structures

Mariona Claret¹ and Álvaro Viúdez¹

Received 21 October 2009; revised 5 July 2010; accepted 23 August 2010; published 23 December 2010.

[1] The interaction between submesoscale baroclinic vortical structures and large amplitude inertia-gravity waves (IGWs), with emphasis on the vertical velocity, is numerically investigated using a high-resolution three-dimensional non-hydrostatic model. A rich variety of vortex-wave interactions are possible depending on the potential vorticity (PV) content and length scale of the submesoscale monopoles or dipoles, and on the amplitude and wave number of the IGWs. On the one hand, large amplitude IGWs cause horizontal and vertical advection of the vortices, which conserve their stability though their geometry is largely modified by the wave motion. On the other hand, the horizontal vortical motion Doppler shifts the local frequency of IGWs. The vortical angular velocity and vortex density stratification lead to a wave dispersion relation involving the *effective* Coriolis frequency (Coriolis frequency plus the vortical angular velocity) and the *total* Brunt-Väisälä frequency. This inhomogeneous change in the local wave frequency causes IGWs to depart from their initial plane geometry. In the particular case of inertial waves, the nonlinear vortex-wave interaction generates spiral IGWs, having vertical velocities one order of magnitude larger than the submesoscale vortical flow in the absence of waves.

Citation: Claret, M., and Á. Viúdez (2010), Vertical velocity in the interaction between inertia-gravity waves and submesoscale baroclinic vortical structures, *J. Geophys. Res.*, 115, C12060, doi:10.1029/2009JC005921.

1. Introduction

[2] Recent numerical works have reproduced the fully three-dimensional nature of submesoscale flows [e. g., *Capet et al.*, 2008], where vertical velocity can reach values one order of magnitude greater than those at the mesoscale [Mahadevan, 2006]. Submesoscale structures have been reported both in the upper ocean [Rudnick and Luyten, 1996; Shay et al., 2003; Capet et al., 2008] and the deep ocean [McWilliams, 1985; Testor and Gascard, 2003; Steffen and D'Asaro, 2004; Kasajima et al., 2006]. On the other hand, inertia-gravity waves (IGWs) are also ubiquitous in the ocean [Garrett and Munk, 1979; Miropol'sky, 2001; Pedlosky, 2003], and consequently interaction between submesoscale flows and IGWs is a frequent phenomenon. Here we address this interaction, focusing on vertical velocity, in the special case where vortical and wave flows have similar amplitudes.

[3] The submesoscale refers to flows with horizontal scales L of order 1–10 km, and Rossby \mathcal{R} and Froude \mathcal{F} numbers also of order 1. Such flows play an important role in the ocean because they facilitate the energy transfer from the mesoscale to smaller scales [Molemaker et al., 2005], and the vertical flux of momentum, buoyancy, potential vorticity (PV), and biogeochemical properties [Lévy et al., 2001; Thomas et al., 2008]. In the deep ocean, long-lived sub-

mesoscale vortices are also responsible for both deep convection [Gascard et al., 2002], and horizontal transport, as they are advected away from their origin by mean currents [Testor and Gascard, 2003].

[4] In the particular case of near-inertial oscillations, anisotropy of the wavefield caused by the mesoscale geostrophic motions has been extensively reported [Moore, 1975a, 1975b; Perkins, 1976; Weller, 1982; Kunze, 1984; van Meurs, 1998; Niwa and Hibiya, 1999]. Several vortex-wave interactions have been proposed to explain this wave heterogeneity, such as wave trapping of IGWs inside vortices [Kunze, 1985], wave capture [Bühler and McIntyre, 2005], dispersion of near-inertial energy by geostrophic eddies [Young and Jelloul, 1997; van Meurs, 1998], inertial pumping [Rubenstein and Roberts, 1986], and resonance mechanisms [Niwa and Hibiya, 1999; Danioux and Klein, 2008b]. Here we address both the vortex-wave mechanisms that explain the wave frequency shift by submesoscale vortices and the PV structures that remain coherent after being advected by large amplitude IGWs. Our results extend the works mentioned above by using a non-hydrostatic numerical model, which considers the fully nonlinear three-dimensional momentum equations and resolves the vertical velocity with high accuracy, to simulate baroclinic asymmetric PV flows of length scales *similar* to those of the pre-existent wavefield.

[5] The first vortex-wave interaction we introduce implies vortical motion affecting plane IGWs. This occurs both through the wave frequency Doppler-shift ($\mathbf{K}_h \cdot \mathbf{u}_{bh}$), where \mathbf{K}_h is the horizontal wave number and \mathbf{u}_{bh} the horizontal

¹Institut de Ciències del Mar, CSIC, Barcelona, Spain.

vortical (balanced) velocity, and through the vortical angular velocity and vortex density stratification anomaly, which lead to *effective* Coriolis and Brunt-Väisälä frequencies [Kunze, 1985]. The second interaction is the advection of the vortical flow by large amplitude IGWs. In this case, the vortex geometry is largely deformed giving rise to new circulation generated in the process toward geostrophic adjustment. Finally, nonlinear vortex-waves interactions trigger a spiral IGW when a pure inertial wave is present in a vortex flow. In this case, horizontal gradients of the vertical vorticity ζ generate gradients in the *effective* Coriolis frequency, through the $\zeta/2$ shift [Mooers, 1975a; Kunze, 1985; Rubenstein and Roberts, 1986] originating a divergence of the wavefield from which vertical velocity develops.

[6] In this work we use a triply periodic nonhydrostatic numerical model under the Boussinesq and f -plane approximations (section 2) to examine the interaction between submesoscale baroclinic vortex structures with Rossby number $\mathcal{R} \lesssim 1$ and pre-existent IGW fields. We particularly focus on the generation of spiral patterns of vertical velocity. The flow has a constant *background* Prandtl ratio $N/f = 10$, where N and f are constant background Brunt-Väisälä and Coriolis frequencies, respectively. We consider two types of vortical structures and waves, namely the monopolar vortex (cyclonic and anticyclonic) and the vortex dipole, as well as two types of waves, namely pure inertial and gravity plane waves (section 3). Next we investigate the flow of a monopole embedded in initially plane inertial and gravity wavefields (sections 4.1 and 4.2). The vortex, although no longer homogeneous nor steady, remains always stable despite substantial advection by large IGWs. Interactions between a submesoscale dipole, the simplest vortical structure having linear momentum, and large amplitude IGWs of different wave numbers are addressed in section 5. The baroclinic dipole remains coherent despite the presence of large amplitude wavefields. The balanced and unbalanced components of the flow are extracted from the *total* flow and are separately analyzed. Finally, conclusions are given in section 6.

2. Numerical Model and Parameters

2.1. $\mathcal{AB}\varpi$ -Model

[7] The non-hydrostatic numerical model (hereinafter referred to as the $\mathcal{AB}\varpi$ -model) simulates the isochoric (volume-preserving) flow of a stratified rotating fluid under Boussinesq and f -plane approximations [Dritschel and Viúdez, 2003]. Here the flow is initialized with (1) a localized vortical flow specified by the potential vorticity (PV) using the PV initialization approach [Viúdez and Dritschel, 2003], and (2) a plane IGW background field (described in section 3.1). The theoretical basis of the numerical model is explained in detail in the references above, and succinctly here in the Appendix with a small lexicon in Table A1. Only a brief definition of the physical quantities is given next.

[8] The Froude number $\mathcal{F} \equiv \omega_h/N$ and the Rossby number $\mathcal{R} \equiv \zeta/f$, where ω_h and ζ are the horizontal and vertical components of the relative vorticity $\boldsymbol{\omega} \equiv \boldsymbol{\omega}_h + \zeta \mathbf{k}$, and N is the *total* Brunt-Väisälä frequency. The vertical displacement of isopycnals is defined as $D(x, t) \equiv z - d(x, t)$, where $d \equiv (\rho - \rho_0)/\rho_z$ is the depth that an isopycnal located at x at time t has

in the reference density configuration defined by $\rho_0 + \rho_z z$. Above $\rho(\mathbf{x}, t)$ is the mass density, and $\rho_0 > 0$ and $\rho_z < 0$ are constant values that do not need to be specified in the Boussinesq approximation. The squared *total* Brunt-Väisälä frequency is therefore

$$N^2(\mathbf{x}, t) = N^2 \left(1 - \frac{\partial D}{\partial z}(\mathbf{x}, t) \right). \quad (1)$$

Static instability occurs when the stratification number $\mathcal{D}_z \equiv \partial D/\partial z > 1$, and inertial instability occurs when $\mathcal{R} < -1$.

[9] The $\mathcal{AB}\varpi$ -model integrates the dimensionless ageostrophic horizontal vorticity $\mathcal{A}_h = (\mathcal{A}, \mathcal{B}) \equiv \tilde{\boldsymbol{\omega}}_h - c^2 \nabla_h D$,

$$\frac{d\mathcal{A}_h}{dt} = -f \mathbf{k} \times \mathcal{A}_h + (1 - c^2) \nabla_h w + \tilde{\boldsymbol{\omega}} \cdot \nabla \mathbf{u}_h + c^2 \nabla_h \mathbf{u} \cdot \nabla D, \quad (2)$$

where $N^2 \equiv -g\rho_z/\rho_0$, the Prandtl ratio $c \equiv N/f$, the relative vorticity $\boldsymbol{\omega} \equiv \nabla \times \mathbf{u}$, the velocity $\mathbf{u} = \mathbf{u}_h + w\mathbf{k}$, ∇ is the gradient operator, subscript h denotes the horizontal component, and $\tilde{\chi} \equiv \chi/f$, for any quantity χ . The material derivative $d\chi/dt \equiv \partial\chi/\partial t + \mathbf{u} \cdot \nabla\chi$. The third prognostic equation is the explicit conservation of PV *anomaly* ϖ through PV contour advection on isopycnal surfaces

$$\frac{d\varpi}{dt} = 0, \quad (3)$$

where

$$\begin{aligned} \varpi &\equiv \Pi - 1 = \frac{\boldsymbol{\omega} + f\mathbf{k}}{f} \cdot \nabla d - 1 = (\tilde{\boldsymbol{\omega}} + \mathbf{k}) \cdot (\mathbf{k} - \nabla D) - 1 \\ &= \tilde{\zeta} - \frac{\partial D}{\partial z} - \tilde{\boldsymbol{\omega}} \cdot \nabla D, \end{aligned} \quad (4)$$

and Π is the *total* PV.

[10] The state variables are the components of the three-dimensional vector potential $\boldsymbol{\varphi} = (\varphi, \psi, \phi)$ which provide the velocity $\tilde{\mathbf{u}} = -\nabla \times \boldsymbol{\varphi}$ and the vertical displacement of isopycnals $D = c^{-2} \nabla \cdot \boldsymbol{\varphi}$. The horizontal components of the vector potential $\boldsymbol{\varphi}_h = (\varphi, \psi)$ are diagnosed every time step by inversion of $\mathcal{A}_h = \nabla^2 \boldsymbol{\varphi}_h$, while the vertical component ϕ is obtained from the inversion of the ϖ definition (4) as a function of (φ, ψ, ϕ) .

2.2. Numerical Parameters

[11] The model domain is a triply periodic box of vertical extent $L_Z = 2\pi$ (which defines the unit of space) and horizontal extents $L_X = L_Y = cL_Z$, where $c = 10$. The number of grid points $(n_X, n_Y, n_Z) = (128, 128, 128)$, and isopycnal surfaces $n_I = 128$. The background Brunt-Väisälä frequency $N = 2\pi$, which defines the background buoyancy period as the unit of time, $T_{bp} \equiv 2\pi/N = 1$. One inertial period $T_{ip} = cT_{bp}$.

[12] All variables are non-dimensional. To recover the physical dimensions of any quantity given the dimensional domain depth H and mean latitude θ_0 , we need to multiply the dimensionless numerical value by the spatial and time-

Table 1. List of Parameters

Case	Number of Vortices	$\varpi_{\min/\max}$	a_x/c	a_y/c	a_z	(ck, cl, m)	$ \mathbf{u}_{th} $	\mathcal{D}_i	$ \mathcal{D}_z _{\max}$	\mathcal{R}_{\min}	\mathcal{F}_{\max}
C1	1	+0.75	1.5	1.5	1.5	(0, 0, 6)	1	-	0.3	-0.53	1.37
C2	1	-0.5	1	1	1	(0, 0, 6)	0.1	-	0.19	-0.42	1.17
C3	1	-0.75	1.5	1.5	1.5	(8, 0, 0)	-	10^{-2}	0.2	-0.63	0.27
C4	1	+0.75	1.5	1.5	1.5	(8, 0, 0)	-	10^{-2}	0.19	-0.05	0.15
C5	2	± 0.75	0.6	0.4	0.4/0.27	-	-	-	0.36	-0.63	0.35
C6	2	± 0.75	0.6	0.4	0.4/0.27	(0, 0, 4)	0.75	-	0.6	-0.87	1.6
C7	2	± 0.75	0.6	0.4	0.4/0.27	(-6, 0, 0)	-	0.2	0.35	-0.68	0.45
C8	2	± 0.75	1.2	0.8	0.8/0.54	(8, 0, 0)	-	10^{-2}	0.39	-0.65	0.40
C9	2	± 0.75	1.2	0.8	0.8/0.54	(-8, 0, 0)	-	10^{-2}	0.39	-0.65	0.37
C10	2	± 0.75	1.2	0.8	0.8/0.54	(0, 8, 0)	-	10^{-2}	0.39	-0.65	0.37

scale conversion factors $S_z = H/\pi$ and $S_t = 1\text{day}/2c\sin\theta_0$, respectively, elevated to the appropriate powers to match the physical dimensions. The time step δt ranges from $\delta t = 0.1$ for slow inertial waves to $\delta t = 10^{-4}$ for large amplitude and fast gravity waves.

3. Initialization

3.1. Wave Initialization

[13] The initial IGW field is set at $t = 0$ from the complex plane wave solutions for the potential components $\hat{\varphi}_i$ in terms of the complex vertical displacement $\hat{\mathcal{D}}_i$, namely

$$\hat{\varphi}_i = \left(\hat{\varphi}_i, \hat{\psi}_i, \hat{\phi}_i \right) = \frac{1}{K_h^2} [\bar{\omega}_l(-l + ik\bar{\omega}_l), \bar{\omega}_l(k + il\bar{\omega}_l), im(1 - c^2)] \hat{\mathcal{D}}_i. \quad (5)$$

Above the complex fields $\hat{\chi} = \hat{\chi}_0 e^{i\theta}$ for any variable χ , where θ is the wave phase, the three-dimensional wave number $\mathbf{K} = (k, l, m) \equiv \nabla\theta$, $K_h \equiv |\mathbf{K}_h|$, and the local frequency $\omega_l \equiv -\partial\theta/\partial t$ satisfies the dispersion relation $\omega_l^2 = (N^2 K_h^2 + f^2 m^2)/K^2$, with $K \equiv |\mathbf{K}|$. These plane IGWs have zero PV anomaly ($\varpi\{\hat{\varphi}_i\} = 0$) and imply

$$\begin{aligned} \hat{\mathbf{u}}_i &= (\hat{u}_i, \hat{v}_i, \hat{w}_i) = \frac{m}{K_h^2} (i\omega_l \mathbf{K}_h + f \mathbf{k} \times \mathbf{K}_h) \hat{\mathcal{D}}_i - i\omega_l \hat{\mathcal{D}}_i \mathbf{k}, \\ \hat{\zeta}_i &= ifm \hat{\mathcal{D}}_i, \quad \hat{\mathcal{D}}_{iz} = im \hat{\mathcal{D}}_i, \end{aligned} \quad (6)$$

so that static stability ($\mathcal{D}_z < 1$) and inertial stability ($\mathcal{R} < -1$) require $m|\hat{\mathcal{D}}_i| < 1$, which is always satisfied in our initial conditions.

[14] The wave potentials $\hat{\varphi}_i$ for a pure gravity wave initialization are obtained from (5) by setting $m = 0$, so that $\omega_l = N$, $\hat{u}_i = \hat{v}_i = 0$, and

$$\hat{\varphi}_i = \left(\hat{\varphi}_i, \hat{\psi}_i, \hat{\phi}_i \right) = \frac{c}{K_h^2} (-l + ikc, k + ilc, 0) \hat{\mathcal{D}}_i. \quad (7)$$

[15] For pure inertial waves $\omega_l = f$ and $\hat{\mathcal{D}}_i = \hat{w}_i = k = l = 0$, so that (5) is not valid. In this case $\hat{\varphi}_i$ is expressed instead in terms of \hat{u}_i as

$$\hat{\varphi}_i = \left(\hat{\varphi}_i, \hat{\psi}_i, \hat{\phi}_i \right) = \frac{1}{fm} (1, -i, 0) \hat{u}_i, \quad (8)$$

and the value \hat{u}_0 is specified by the initial conditions.

3.2. Vortex Initialization

[16] The vortex initialization procedure is required to avoid the initial generation of IGWs during the geostrophic adjustment. This is specially important for w which, having an amplitude several orders of magnitude smaller than $|\mathbf{u}_h|$, would be largely interfered by horizontal imbalanced motions. The initialization procedure [Viúdez and Dritschel, 2003] is based on the slow, progressive growth of the PV anomaly field $\varpi(\mathbf{X}, t)$ in every fluid particle \mathbf{X} , that is, in a Lagrangian way during a time interval from $t = 0$ (when $\varpi(\mathbf{X}, 0) = 0$) to $t = t_i$ (when $\varpi(\mathbf{X}, t_i) = \varpi_0(\mathbf{X})$ is the prescribed PV anomaly). The initialization is done in the presence of IGWs over a time period of $t_i = 5T_{ip}$, which has been found to be sufficient to avoid significant excitation of IGWs. In the case of initialization with large amplitude plane gravity waves there is no need for a smooth initialization of the vortical motion since the w of the IGWs already present is several orders of magnitude larger than the w of the waves due to the initial imbalance. In these cases shorter initialization periods are chosen, ranging from $t_i = 0.2T_{ip}$ to $t_i = 0.5T_{ip}$.

4. Vortex-Wave Interaction

[17] The interaction between a submesoscale monopole (cyclone and anticyclone) and large amplitude IGWs (a pure inertial and gravity wave) is first investigated in order to understand how this interaction occurs in more complex vortical structures like the vortex dipole. The dipolar vortex is of special interest because it is the simplest vortical structure with net linear momentum. A list of the vortices parameters (ϖ minima or maxima and the maximum lengths of the semiaxes of the ellipsoids of constant PV of the vortices a_x , a_y , and a_z), wave properties (\mathbf{K} , \mathbf{u}_{th} and \mathcal{D}_i), and flow numbers (\mathcal{D}_z maxima, \mathcal{R} minima, and \mathcal{F} maxima) of the simulations is given in Table 1. In all cases the flow remains statically and inertially stable.

[18] In this section we analyze the interaction between waves and baroclinic axisymmetric monopoles, which have $w = 0$ at $t = 0$, of similar length and velocity amplitude. As a result of this interaction, the vortex geometry is largely modified by inertial (section 4.1) or gravity (section 4.2) wave flows.

4.1. Vortex and Inertial Waves Interaction

[19] We consider here the interaction between a vortex and an inertial wavefield of similar velocity amplitude. An initially axisymmetric cyclone with $\varpi_{\max} = 0.75$ and hori-

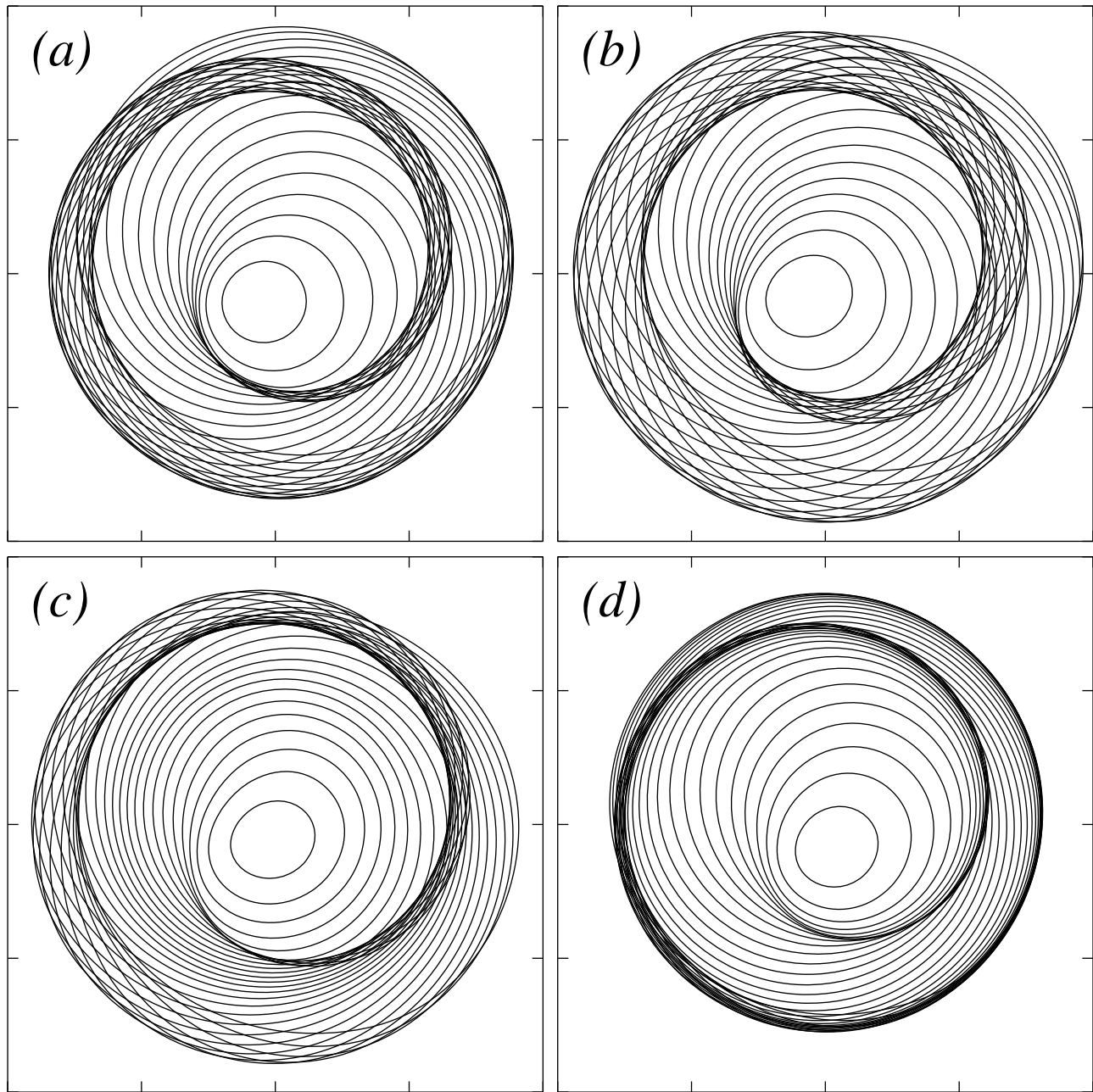


Figure 1. Time sequence of the outer potential vorticity (PV) contour in every isopycnal of the lower half of the vortex, from the middle isopycnal $i_l = 65$ (contours with larger radius) to $i_l = 46$, the deepest isopycnal with $\varpi \neq 0$ (contours with shorter radius). Time is (a) $t = 5T_{ip}$, (b) $t = 5.25T_{ip}$, (c) $t = 5.5T_{ip}$, and (d) $t = 5.75T_{ip}$. The horizontal extent is $\delta x = \delta y = 1.5c$.

zonal a_h and vertical a_z radii $a_h/c = a_z = 1.5$ (case C1) is initialized, as described in section 3.2, during $t_i = 5T_{ip}$ in a field of inertial waves (section 3.1) of horizontal velocity amplitude $|\mathbf{u}_{ih}| = 1$ and vertical wave number $m = 6$ (wavelength $\lambda_z = 2\pi/m \simeq 1$).

[20] The inertial wave causes horizontal advection of the vortex, which is horizontally displaced, completing a cycle every inertial period (Figure 1). Because λ_z and a_z are similar, the vertical shear of the wave distorts the vortex, which no longer remains spherical in the QG space (Figure 1).

The $|\mathbf{u}_h|$ of the waves is similar to the $|\mathbf{u}_h|$ of the vortical flow altogether reaching $total |\mathbf{u}_h|_{max} = 1.80$ at $t = 8.5T_{ip}$. This implies that the spatially homogeneous but time rotating inertial wave flow is also largely distorted by the spatially inhomogeneous (circular) but steady vortical flow. As a result the total flow is neither spatially homogeneous nor steady (Figure 2).

[21] The initially straight inertial wave phase lines are curved by the vortex also in the vertical plane. This effect is explained by the modification of the local wave frequency

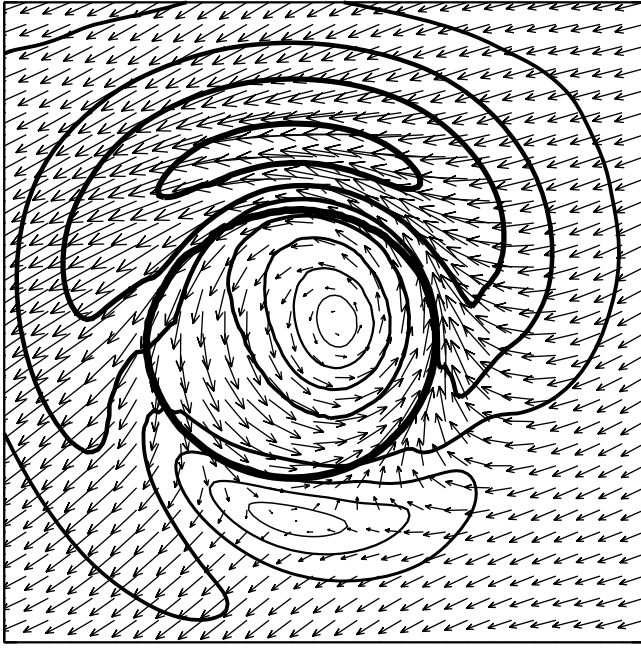


Figure 2. Horizontal velocity \mathbf{u}_h ($|\mathbf{u}_h|_{\max} = 1.49$, $\delta|\mathbf{u}_h| = 0.25$) at $t = 5.5T_{ip}$ and $i_z = 65$ ($z = 0$). PV contour $\varpi = 0.22$ at $z = 0$ (thick contour) is included. Domain extent is $\delta x = \delta y = 5.8c$. Only every fourth vector is represented.

ω_l in the vortex-wave interaction region. Splitting the total velocity \mathbf{u} into a wave component \mathbf{u}_i plus a vortical (balanced) component $\mathbf{u}_{bh}(\mathbf{x}_h, z) = \Omega(z) \mathbf{k} \times \mathbf{x}_h$ (subscripts i and b , respectively) of a rigid rotation with angular velocity $\Omega(z)$

in the basic flow equations (A4)–(A7), the wave dynamics satisfies at $x \cong y \cong 0$ the equations

$$\begin{aligned} \frac{\partial \mathbf{u}_i}{\partial t} + f_e \mathbf{k} \times \mathbf{u}_i &= -\alpha_0 \nabla p_i - N^2 \mathcal{D}_i \mathbf{k}, \\ \frac{\partial \mathcal{D}_i}{\partial t} + w_i \frac{\partial \mathcal{D}_b}{\partial z} &= w_i, \\ \nabla \cdot \mathbf{u}_i &= 0, \end{aligned} \quad (9)$$

where $f_e(z) \equiv f + \Omega(z)$ is the *effective* Coriolis frequency.

[22] The new dispersion relation is obtained substituting the plane wavefields $\tilde{\chi}(\mathbf{x}, t) = \tilde{\chi}_0 e^{i(\mathbf{K}\mathbf{x} - \omega t)}$ into (9), yielding

$$\omega_l^2 = \frac{\mathcal{N}^2 K_h^2 + f_e^2 m^2}{K^2}, \quad (10)$$

where ω_l is the local frequency, and $\mathcal{N}^2 \equiv -\alpha_0 g \partial \rho / \partial z = N^2 (1 - \partial \mathcal{D} / \partial z)$ the *total* Brunt-Väisälä frequency.

[23] In the cyclone case (C1) an *effective* wave frequency $\omega_l \cong 0.13$ is predicted from (10). This is confirmed by numerical results which show that the wave frequency peak evolves from inertial $\omega_l = 0.1$ to near-inertial frequency $\omega_l = 0.12 \pm 0.01$ (Figure 3). The local frequency shift $\zeta/2$ [Mooers, 1975a; Kunze, 1985; Rubenstein and Roberts, 1986] is also caused by baroclinic PV structures that remain no longer *axisymmetric* after the vortex-wave interaction.

[24] In order to analyze how the balanced flow affects the wave motion and vice versa, we have extracted the balanced flow from the *total* flow. The *balanced* vector potential $\varphi_b = (\varphi_b, \psi_b, \phi_b)$ is here diagnosed using the Optimal PV Balance (OPVB) approach [Viúdez and Dritschel, 2004], and the balanced quantities are derived therefrom. From a given PV field *anomaly* $\varpi(x, y, z)$, the OPVB approach diagnoses a

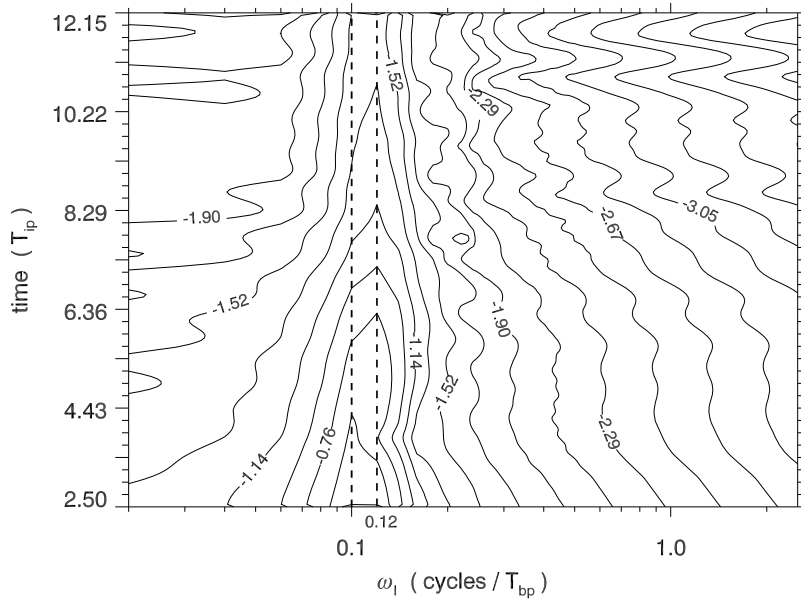


Figure 3. Clockwise rotatory spectrogram of $u + iv$. The spectrogram comprises 194 spectra from $t = 0$ to $t = 14.25T_{ip}$ using a window of $5T_{ip}$ and a time lag of $\delta t = 0.5T_{bp}$. The distribution shows the Fourier transform magnitude of the components $\sqrt{\hat{u}^2(\omega_F) + \hat{v}^2(\omega_F)}$ for the Fourier frequencies $\omega_F < 0$. The initial inertial peak evolved to near-inertial, $\omega_l = 0.12 \pm 0.01$.

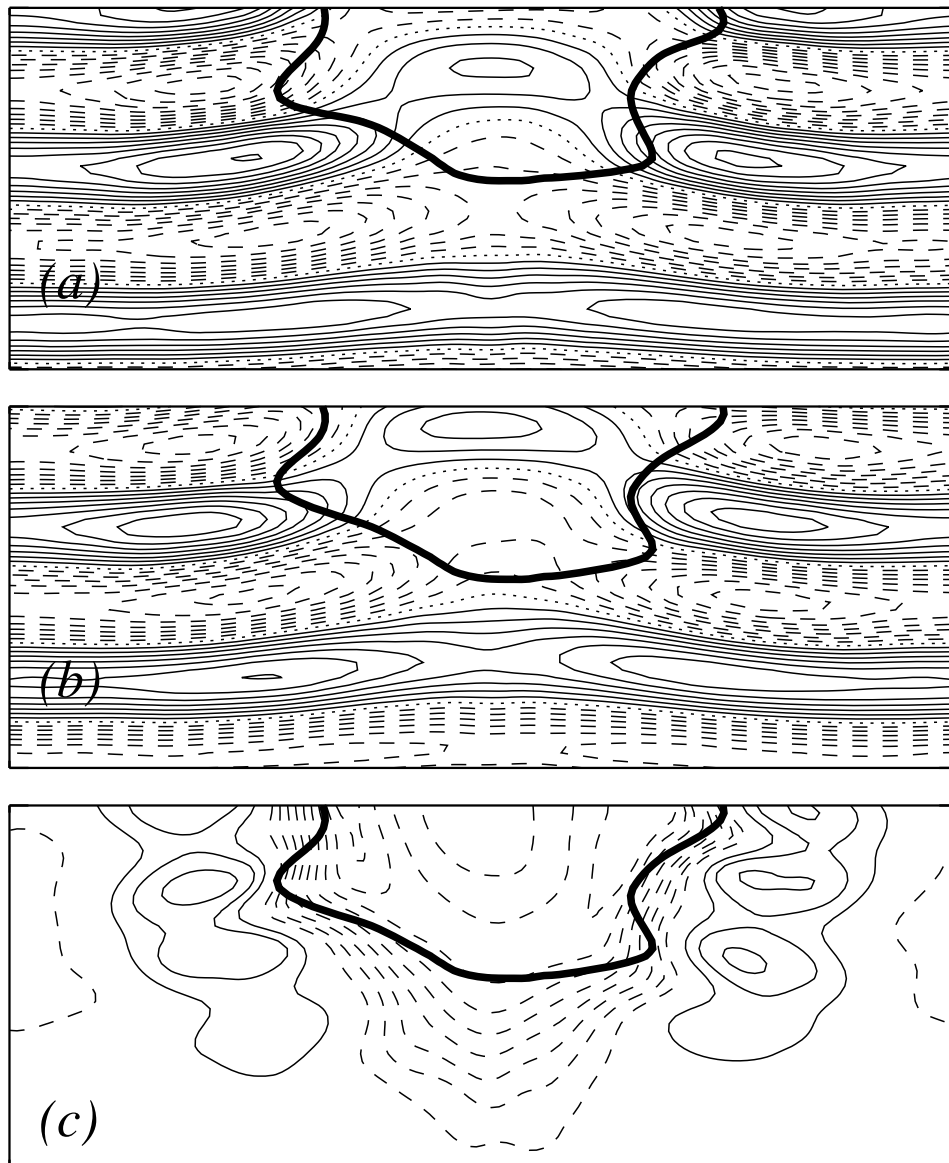


Figure 4. Vertical distributions in the x - z plane $i_Y = 65(y = 0)$ at $t = 5T_{ip}$ of (a) u_i ($u_i \in [-1.3, 1.28]$, $\delta u_i = 0.15$), (b) v_i ($v_i \in [-1.17, 1.19]$, $\delta v_i = 0.15$), and (c) the speed anomaly of the unbalanced horizontal velocity $U_i = |\mathbf{u}_i| - 1$ ($U_i \in [-0.82, 0.31]$, $\delta U_i = 0.09$). Domain extent is $x \in [-\pi, \pi]e$, $z \in [-3/4\pi, 0]$. The PV contour $\varpi = 0.2$ (thick line) is included for reference. Hereinafter, solid and dashed lines indicate positive and negative values, respectively.

flow having only those IGWs that have been spontaneously generated during the process of acquiring its own PV (i.e., during a time interval set equal to the initialization time $t_i = 5T_{ip}$). The OPVB flow does not contain most of the IGWs, which remain, almost entirely, in the *unbalanced* vector potential $\varphi_i \equiv \varphi - \varphi_b$. The unbalanced velocity and vertical displacement of isopycnals are obtained directly from φ_i through the usual relations $\mathbf{u}_i = -f\nabla \times \varphi_i$ and $\mathcal{D}_i = -\epsilon^2 \nabla \cdot \varphi_i$, respectively. An alternative way to obtain the interaction between the inertial waves and the vortical flow in this case is using the near-inertial oscillation (NIO) equation of [Young and Jelloul, 1997], which is valid for small Rossby numbers. We note that their geostrophic stream function Ψ

is similar to our vertical potential ϕ . However, we use here the OPVB because it is valid for largely ageostrophic flows.

[25] The wave frequency shift mentioned before is noticeable because the vertical wave phase velocity at the vortex center ($\sigma_Z = (f + \Omega)/m$) is larger than outside the vortex ($\sigma_Z = f/m$). Therefore, phase lines of \mathbf{u}_i at $x \cong y \cong 0$ accelerate inside the vortex (Figures 4a and 4b). As a result, the originally straight phase lines of \mathbf{u}_{ih} are broken by the cyclone, and the vertical distribution of the speed anomaly of the unbalanced horizontal velocity is distorted (Figure 4c), reaching negative values at the vortex center.

[26] As we have seen, the initial inertial wavefield is strongly modified by the vortex, but at the same time the

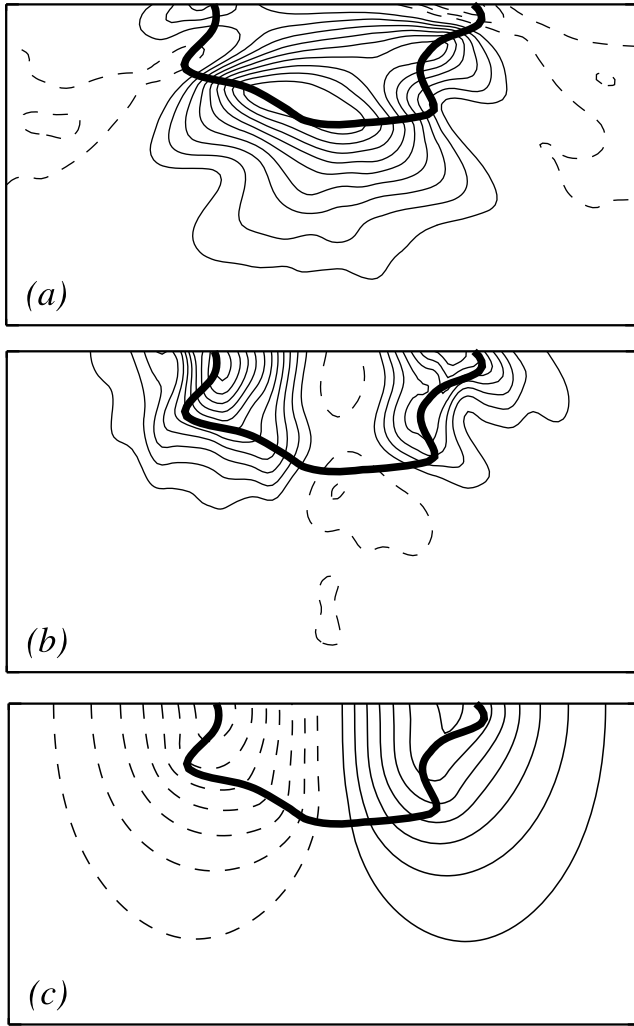


Figure 5. Vertical distributions in the x - z plane at $i_y = 65$ ($y = 0$) and $t = 5T_{ip}$ of the (a) isopycnal displacement \mathcal{D} ($\mathcal{D} \in [-0.06, 0.17]$, $\delta\mathcal{D} = 0.017$), (b) horizontal geostrophic speed anomaly $U^{g'} = |\mathbf{u}_h^g| - 1$ ($U^{g'} \in [-0.15, 0.82]$, $\delta U^{g'} = 0.07$), and (c) balanced v ($v_b \in [-1.55, 1.18]$, $\delta v_b = 0.15$). Domain extent is $x \in [-\pi, \pi]c$, $z \in [-\pi, 0]$. The PV contour $\varpi = 0.2$ is included.

vortex is also deformed by the wave velocity, which causes the PV contours to depart from the spherical geometry, modifying the vertical distribution of \mathcal{D} (Figure 5a). Since \mathcal{D} is related to the geostrophic velocity shear $\mathbf{u}_{hz}^g \equiv \partial\mathbf{u}_h^g/\partial z$ by the thermal-wind relation

$$\mathbf{u}_{hz}^g = -\frac{N^2}{f}\mathbf{k} \times \nabla_h \mathcal{D}, \tag{11}$$

the $|\mathbf{u}_h^g|$ contours (Figure 5b) depart from the circular geometry typical of a vortex in the absence of a wavefield. This is also confirmed when extracting the balanced flow from the total flow (Figure 5c).

[27] An important result of the vortex-wave interaction is the generation of w in the form of spiral waves (Figure 6). Since the motion of the isolated spherical vortex on the one

hand, and the motion of the isolated inertial waves on the other hand, are purely horizontal, the development of w in the vortex-wave system is a clear result of *nonlinear* vortex-wave interaction.

[28] The maximum w amplitude reaches $|w|_{\max} = 5 \times 10^{-2}$, that is 5% of the horizontal inertial wave speed, from $t = 5T_{ip}$ to $t = 6T_{ip}$ (Figures 6a and 6b). This spiral w pattern seems to be related to wave motion rather than to balanced motion. The Quasi-Geostrophic (QG) vertical velocity w^g is

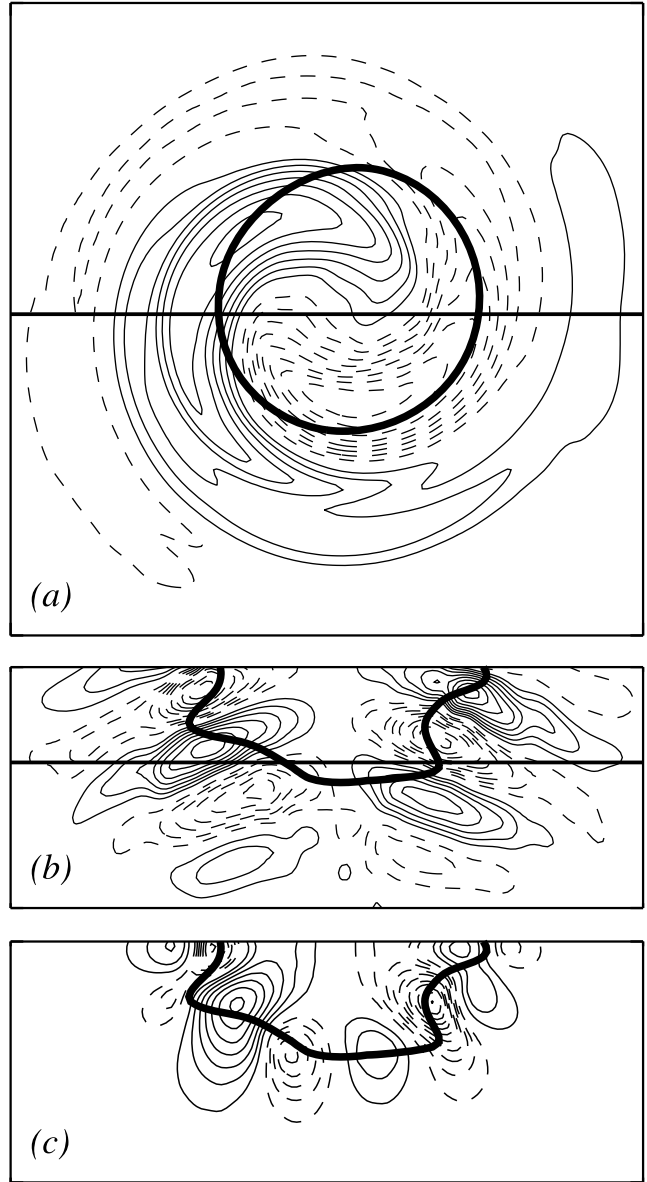


Figure 6. Distributions of total vertical velocity w ($w \in [-4.81, 4.23] \times 10^{-2}$, $\delta w = 5 \times 10^{-3}$) at $t = 5T_{ip}$ for (a) the x - y plane at $i_z = 45$ ($z = -0.98$) and (b) the x - z plane at $i_y = 65$ ($y = 0$). (c) Vertical distribution at the same time of w_b ($w_b \in [-5.52, 3.6] \times 10^{-4}$, $\delta w_b = 5 \times 10^{-5}$). Domain extent is $x, y \in [-\pi, \pi]c$, $z \in [-3/4\pi, 0]$. PV contour $\varpi = 0.2$ (thick line) is included. Straight lines mark the horizontal (Figure 6a) and vertical (Figure 6b and 6c) sections plotted.

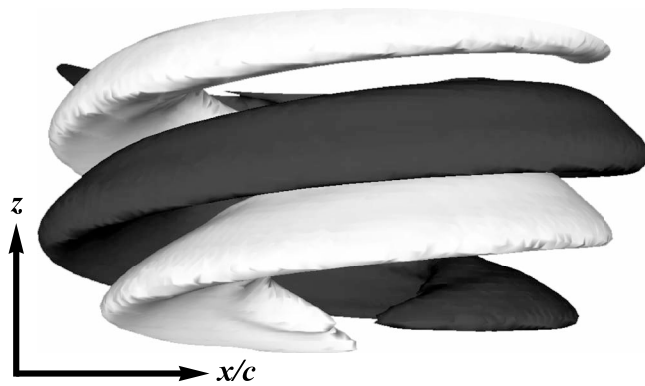


Figure 7. Isosurfaces of *total* vertical velocity w ($w = \pm 0.02$) at $t = 5T_{ip}$. The view is from the south.

obtained by solving the QG omega equation [Hoskins *et al.*, 1978]

$$c^2 \nabla_h^2 w^g + \frac{\partial^2 w^g}{\partial z^2} = 2 \nabla_h \cdot \mathbf{Q}_h^g, \quad (12)$$

where $\mathbf{Q}_h^g \equiv c^2 \nabla_h \mathbf{u}_h^g \cdot \nabla_h \mathcal{D}$ is the geostrophic \mathbf{Q} -vector and \mathbf{u}_h^g is the geostrophic velocity. Though having a spiral pattern as well, w^g is about one order of magnitude smaller than the total w (not shown). The unbalanced origin of the *total* w is confirmed by splitting it into w_b and w_i using the OPVB approach. The vertical distribution of w (Figure 6b) follows the pattern of w_i and both have the same order of magnitude, which is two times larger than that of w_b (Figure 6c). The motion of the spiral IGWs is that of a right-handed helix (the height increasing with increasing phase, Figure 7), rotating anticyclonically so that the phases propagate upward. The

wave packet propagates downward and horizontally leaving the vortical region in a few inertial periods (not shown).

[29] This spiral IGW has a local frequency ranging from f to f_e at initial times and extending to $2f$ and $3f$ frequencies afterward (Figure 8). Near-inertial w is generated by divergence of the \mathbf{u}_i field, which becomes horizontally inhomogeneous because ζ shifts the frequency of pure inertial waves. When separating unbalanced from balanced flows we observe that ζ_i and ζ_b have the same order of magnitude after $t > t_i$. On the one hand, ζ_i is in phase with w (not shown), as predicted from (6). However pure inertial waves have $\zeta_i = 0$ at $t = 0$. On the other hand, we observe that w correlates with $|\nabla \zeta_b|$ maxima after $t > t_i$ and in deeper layers, where horizontal advection is minimum (Figure 9a). As a result, w_i develops at vortex edges (note that $\mathcal{F} > 1$, $\mathcal{F}_{\max} = 1.37$, occurs once the spiral wave has been already generated). Since the vortex geometry is largely horizontally advected by an initially pure inertial wave, $|\nabla \zeta_b|$ isosurfaces become spiralized with depth (Figure 9b) generating a helical IGW. Thus, while the frequency of the *total* w is directly related to ζ , its three-dimensional structure is explained by $|\nabla \zeta_b|$, in accordance with the stated correlation between w and the eddy relative vorticity [Danioux and Klein, 2008a]. Finally, superinertial w observed at later times is due to resonance mechanisms, in agreement with the results of [Niwa and Hibiya, 1999] and [Danioux and Klein, 2008b], that occur when PV structures and IGWs have similar length scales.

[30] Analogous results were obtained with an *axisymmetric* anticyclone (Table 1, case C2), having $\varpi_{\min} = -0.5$ and semiaxes $a_h/c = a_z = 1$, initialized with an inertial wavefield of $|\mathbf{u}_{ih}| = 0.1$ and $m = 6$ (wavelength $\lambda_Z \cong 1$). In this case the vortex has $\Omega < 0$ and the local frequency $\omega_l \cong 0.79 < f$. Consequently, σ_Z at the vortex center is smaller than that far

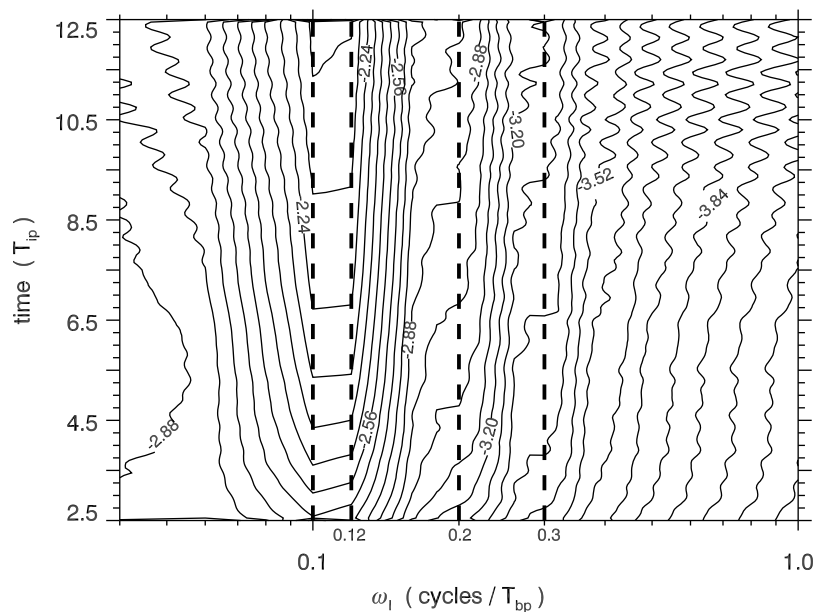


Figure 8. Domain-averaged spectrogram $w(\omega_l, t_k) \equiv \frac{1}{n} \sum_{j=1}^n \hat{w}(\mathbf{x}_j, \omega_l, t_k)$ from $t = 0$ to $t = 15T_{ip}$, where $\hat{w}(\mathbf{x}_j, \omega_l, t_k)$ is the Fourier transform of the time series $w(\mathbf{x}_j, t)$ with $t \in [t_k - \Delta_t/2, t_k + \Delta_t/2]$. The spatial average comprises $n = 8^3$ time series equally distributed in the three-dimensional domain. The spectrogram window is $\Delta_t = 5T_{ip}$ and the time lag $\delta_t = 0.5T_{bp}$. The vertical dashed lines mark frequencies $f, f + \zeta/2 \cong 0.12, 2f$, and $3f$.

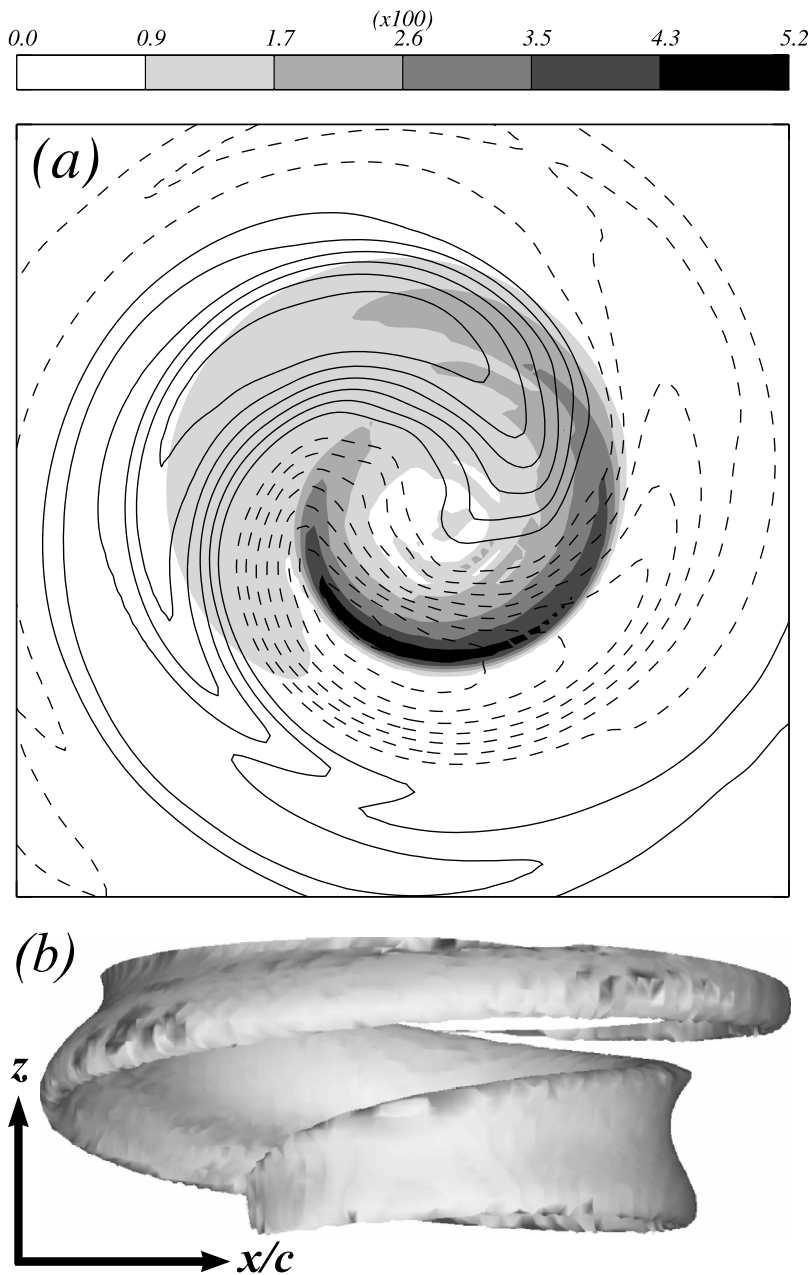


Figure 9. (a) As in Figure 6, but at $i_z = 43$ ($z = -1.03$) ($w \in [-4.18, 3.48] \times 10^{-2}$, $\delta w = 5 \times 10^{-3}$). Shaded contours are $|\nabla_h \zeta_b|$ (max = 5.1×10^{-2} , $\Delta = 8.7 \times 10^{-3}$). Domain extent is $x, y \in [-3/4\pi, 3/4\pi]$. (b) Isosurface $|\nabla_h \zeta_b| = 0.04$ at the same time $t = 5T_{ip}$. The view is from the south.

away from it, which is the opposite effect to that described in the cyclonic case, and wave phase lines accumulate at eddy edges (Figure 10a). The *total* w also shows a right-handed helical structure (not shown), consistent with the anticyclonic rotation with time of the inertial wave velocity, which propagates horizontally and downward at initial times but it is trapped at the eddy bottom later on (Figures 10b–10d). This spiral IGW has a subinertial frequency $\omega_l \simeq 0.08 \pm 0.01$ (Figure 11) and therefore is close to the predicted f_e .

[31] Though we do not consider in detail the long term vortex-wave interaction, we note that, starting at $t = 8.25T_{ip}$ and during the next $16T_{ip}$, the inertial waves may cause the vortex to become unstable in the sense that the vortex losses

PV by PV filamentation (not shown). This PV filamentation increases the horizontal PV gradients remaining in the vortex and, as a result, later on at $t = 13.43T_{ip}$ the flow becomes inertially unstable ($\mathcal{R} < -1$). This long term instability is left for future research.

4.2. Vortex and Gravity Waves Interaction

[32] In this section a spherical (in the QG space) anticyclone, having $\varpi_{\min} = -0.75$ and semiaxes $a_h/c = a_z = 1.5$ in the initial configuration, is initialized (Figure 12a) embedded in a gravity wavefield with $k = 8/c$ (wavelength $\lambda_x/c = 2\pi/(ck) \simeq 0.78$) and $\mathcal{D}_i = 10^{-2}$ (case C3, Figure 12b). Thus, the wave spatial scale is smaller, though of the same order,

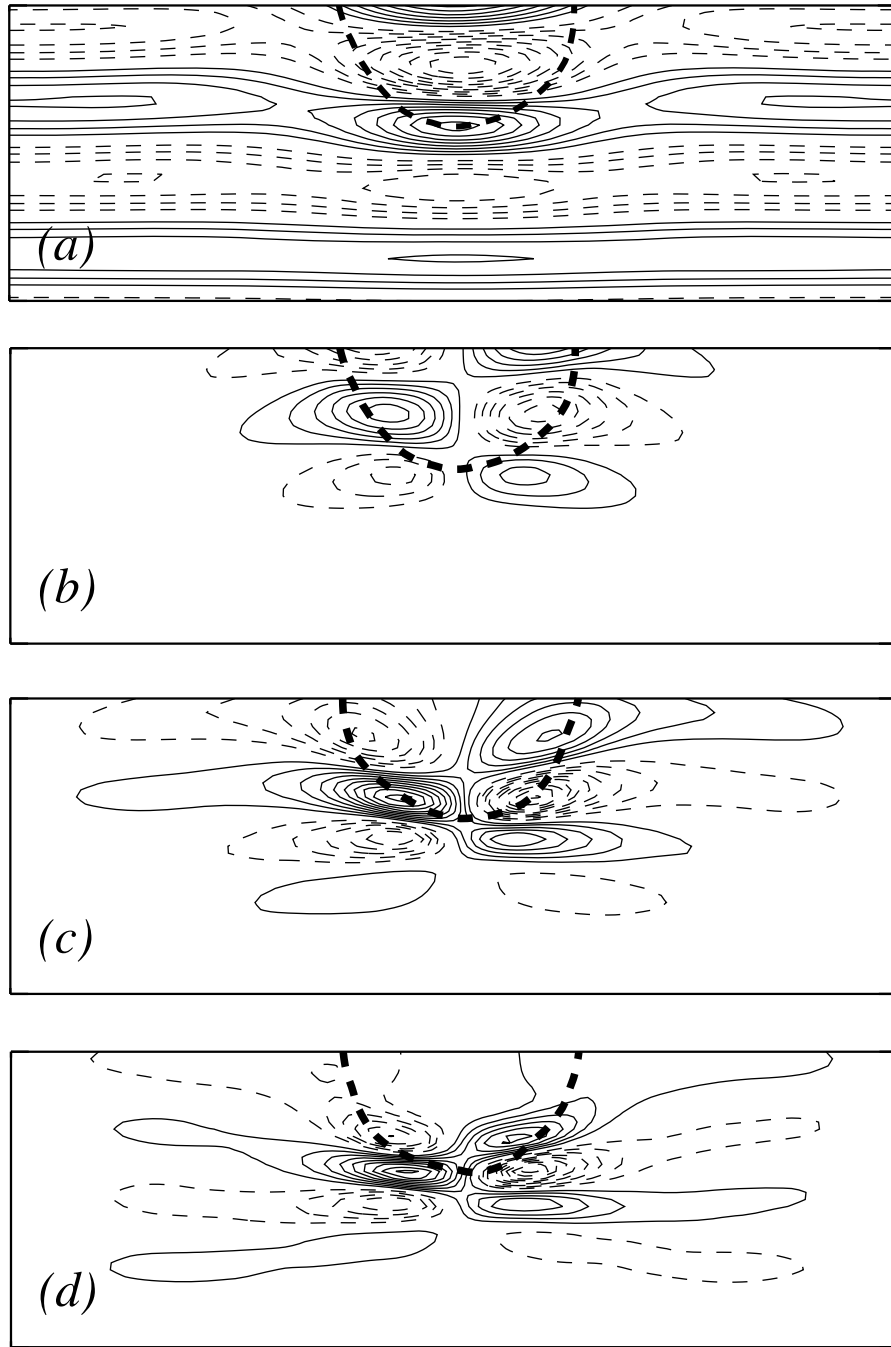


Figure 10. Vertical distributions at $i_Y = 65$ ($y = 0$) of (a) $v_i(x, z)$ ($v_i \in [-0.24, 0.2]$, $\delta v_i = 0.025$) at $t = 5T_{ip}$ and of total $w(x, z)$ ($w \in [-8.5, 8.7] \times 10^{-3}$, $\delta w = 8.3 \times 10^{-4}$) at (b) $t = 5T_{ip}$, (c) $t = 5T_{ip}$, and (d) $t = 15T_{ip}$. PV contour $\varpi = -0.2$ is included (solid thick line). The domain extent is $x \in [-\pi, \pi]c$, $z \in [-2/3\pi, 0]$.

than the vortical flow scale. Note that the vortical \mathcal{D} (due to the otherwise balanced vortex) is zero at $z = 0$. The maximum amplitude of \mathcal{D} caused by the vortical motion is $|\mathcal{D}_b|_{\max} = 0.20$ at the end of the initialization period (Figure 12c), which is about 20 times larger than \mathcal{D}_i . However, the amplitude of the vertical wave motion is $w_i = 0.06$, which is 10 times larger than the typical mesoscale QG vertical velocity w^q (i.e., w^q is about 10^{-3} times the horizontal vortical speed).

[33] The most noticeable result is the deformation of the initially straight phase lines of w of the gravity waves

(Figure 13). This occurs because the oscillating fluid particles are horizontally advected by the vortex giving a new local (absolute) wave frequency ω_l which is the Doppler-shifted particle (intrinsic) wave frequency ω_p by the vortex motion, according to

$$\omega_l = \omega_p + \mathbf{K}_h \cdot \mathbf{u}_{bh}. \tag{13}$$

Since $|\mathcal{D}_z|_{\max} = 0.2$, we have $\mathcal{N} \cong N$, and thus ω_p is approximately homogeneous. Consequently, ω_l is affected

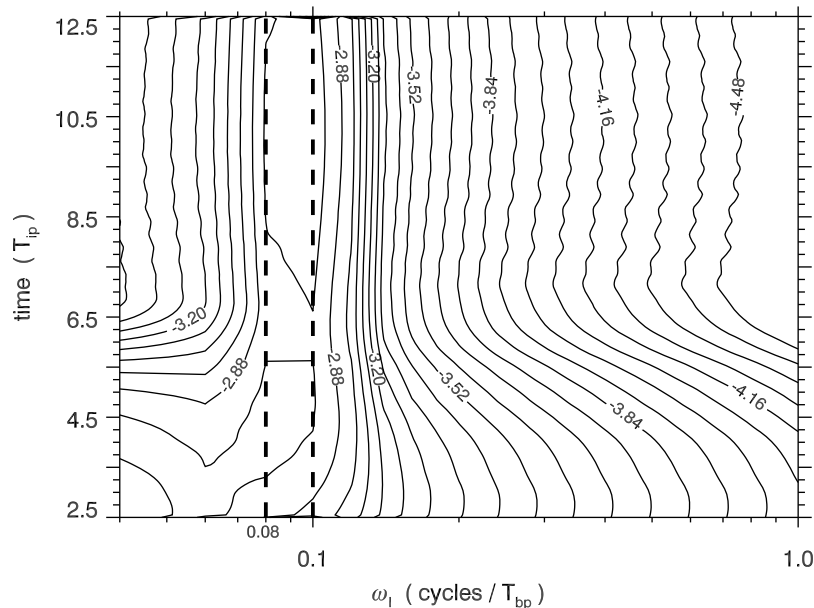


Figure 11. Domain-averaged spectrogram $w(\omega_l, t_k)$ as in Figure 8. Spatial average comprises $n = 9^2 \times 17$ horizontal points equally distributed over 17 vertical levels. In this case vertical dashed lines mark frequencies f and $f - \zeta/2 \cong 0.08$.

mainly by the Doppler shift $\mathbf{K}_h \cdot \mathbf{u}_{bh}$. The anticyclonic vortical motion $\mathbf{u}_{bh} = u_b \mathbf{i} + v_b \mathbf{j}$ has $u_b > 0$ ($u_b < 0$) at $y > 0$ ($y < 0$), implying a positive (negative) frequency Doppler shift. Hence ω_l increases (decreases) in the northern (southern) region of the vortex, so that the initially straight phase lines acquire an anticyclonic pattern.

[34] The deformation of wave phase lines caused by the vortex is not confined to the vortical region, but is transferred through all of the water column (Figure 13). As a first approximation we assume that the vortical vertical motion can be neglected, so that $\nabla_h \cdot \mathbf{u}_{bh} = 0$, since $\mathbf{u}_{ih} = \mathbf{0}$ for gravity waves, and the nondivergence condition yields $\partial w / \partial z = 0$. Therefore the horizontal phase velocity $\sigma_h \equiv (-\partial w / \partial t) / |\nabla_h w|$ is constant throughout the water column, $\partial \sigma_h / \partial z = 0$.

[35] Similar results were obtained for a cyclone with $\varpi_{\max} = 0.75$ and semiaxes $a_h/c = a_z = 1.5$ in a gravity wavefield identical to the case above (case C4, not shown). In this case the initial configuration has $|D|_{\max} = 0.18$, that is, 18 times larger than D_i . Contrary to the anticyclonic case, the initially straight phase lines acquire a cyclonic pattern because now ω_l decreases (increases) in the northern (southern) side of the vortex due to the Doppler shift frequency (13).

5. Dipole-Wave Interaction

[36] We address here the interaction between a vortex dipole, which, unlike the monopolar vortex, possesses a net linear momentum, and large amplitude IGWs. With that purpose we first describe the flow characteristics of a dipole (section 5.1) initialized when pure inertial wave (section 5.2) or gravity wave (section 5.3) fields are included.

5.1. The Dipole

[37] A submesoscale baroclinic dipole is here initialized, in the absence of waves, as two ellipsoidal PV distributions with $\varpi_{\max} = 0.75$ and $\varpi_{\min} = -0.75$, horizontal semiaxes

$a_x^\pm = 0.6c$ and $a_y^\pm = 0.4c$, and vertical semiaxes $a_z^+ = 0.4$ and $a_z^- = 0.27$ for the cyclone (+) and the anticyclone (-), respectively (case C5, Figure 14a). The initial asymmetry in the prescribed a_z^\pm is due to the fact that these vortices are defined in the initial (reference) configuration which has flat isopycnals. During the initialization time the isopycnals stretch (shrink) in the anticyclone (cyclone), so that at the end of the initialization period ($t_i = 5T_{ip}$) the vortices have a similar vertical extent in the physical space and the dipole describes a straight trajectory [Dubosq and Viúdez, 2007]. The horizontal velocity, which is slightly larger in the anticyclone than in the cyclone, reaches maxima $|\mathbf{u}_h|_{\max} = 0.78$ at the dipole center (Figure 14b). The vertical velocity (Figure 14c) is three orders of magnitude smaller than $|\mathbf{u}_h|$, and has the typical quadrupolar pattern of mesoscale QG dipoles [Pallás-Sanz and Viúdez, 2007].

5.2. Dipole and Inertial Waves Interaction

[38] The baroclinic dipole described above is initialized, according to section 3.2, embedded in an inertial plane wavefield (section 3.1) with $m = 4$ (wavelength $\lambda_z = 2\pi/m \cong 1.57$) and speed $|\mathbf{u}_{ih}| = 0.75$, case C6. Thus, λ_z is about twice the vortex vertical extent $2a_z \cong 0.7$. Nevertheless, despite the large wave amplitude, the dipole remains coherent as a stable structure during many inertial periods.

[39] As a result of the dipole-wave interaction the total $|\mathbf{u}_h|$ reaches $|\mathbf{u}_h|_{\max} = 1.5$, which approximately corresponds to the sum of the wave ($|\mathbf{u}_{ih}|_{\max} = 0.75$) and dipole ($|\mathbf{u}_{bh}|_{\max} = 0.78$) speeds that were separately considered. Since the inertial wavefield has homogeneous speed, the extreme values of $|\mathbf{u}_h|_{\max}$ occur along the dipole axis, being maxima or minima depending on the phase of the waves (Figure 15a). Initially straight u and v phase lines (see vertical sections in Figures 15b and 15c) are displaced up (down) in the cyclone (anticyclone). This feature is consistent with the explanation given

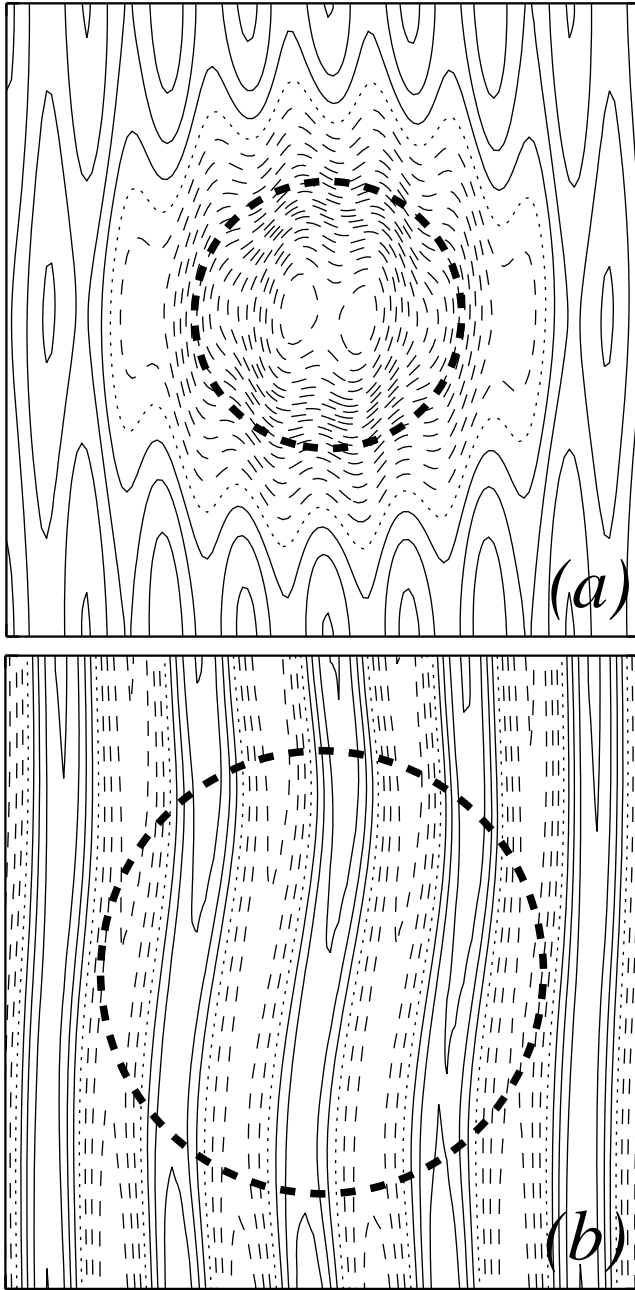


Figure 12. Distributions at $t = 4T_{bp}$ of the vertical displacement \mathcal{D} at (a) $i_z = 40$ ($z = -1.2$, $\mathcal{D} \in [-18, 4.2] \times 10^{-2}$, $\delta\mathcal{D} = 1 \times 10^{-2}$) and (b) $i_z = 65$ ($z = 0$, $\mathcal{D} \in [-1, 1] \times 10^{-2}$, $\delta\mathcal{D} = 2.5 \times 10^{-3}$). The PV contour $\varpi = -0.2$ at $z = 0$ is included. The domain extent is $\delta x = \delta y = 2\pi c$ in (Figure 12a), and $\delta x = \delta y = 3.62c$ in (Figure 12b).

in section 4.1 for the interaction between a monopolar vortex and inertial waves.

[40] In this interaction the vortex geometry is less deformed by the wave flow than in the monopole-wave case (Figure 4) because $a_z < \lambda_z$. Consequently, when applying the aforementioned OPVB method (section 4.1), the pattern of the balanced horizontal \mathbf{u}_{bh} and vertical velocity w_b are little distorted by the wavefield, despite the large wave velocity, and adjust to the typical horizontal and vertical

velocity patterns of the dipole in the absence of waves (Figures 16a and 16b). The amplitude of w_b is, however, about twice that of w in the case of the dipole without waves (Figure 14c).

[41] In contrast, a dipole-wave interaction clearly occurs in \mathbf{u}_i (Figures 16c and 16d), with $|\mathbf{u}_{ih}|$ changing by 13.5% at $z = 0$ in the vortices and with the largest phase change happening in the anticyclone (Figure 16c). At the depth of maximum w ($z = -0.15$) w_i is very large (Figure 16d), of about one order of magnitude larger than w_b (Figure 16b), and is about 20 times larger than the w of the dipole in absence of waves. Thus, the interaction between the vortices and the inertial waves enhances the vertical velocity. The horizontal pattern of w_i at $z = -0.15$ (Figure 16d) corresponds to the upper distribution of the interaction between two near-inertial waves triggered in the monopoles after $t > t_i$ (Figure 7, section 4.1). The resulting IGW has downward wave packet propagation and a spiral pattern can be noticed in horizontal distributions of w_i at deeper layers

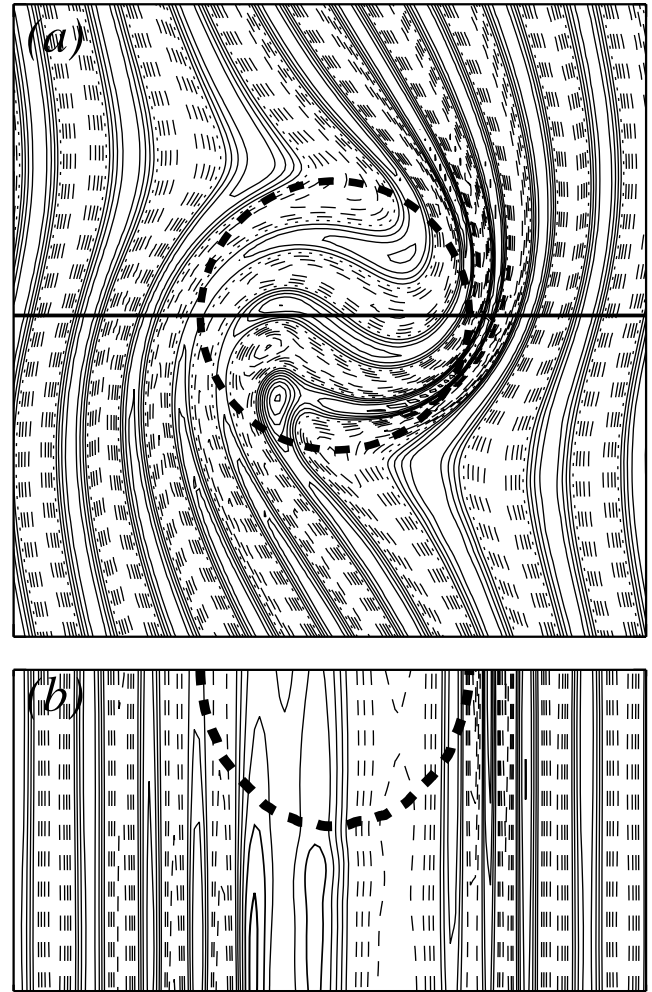
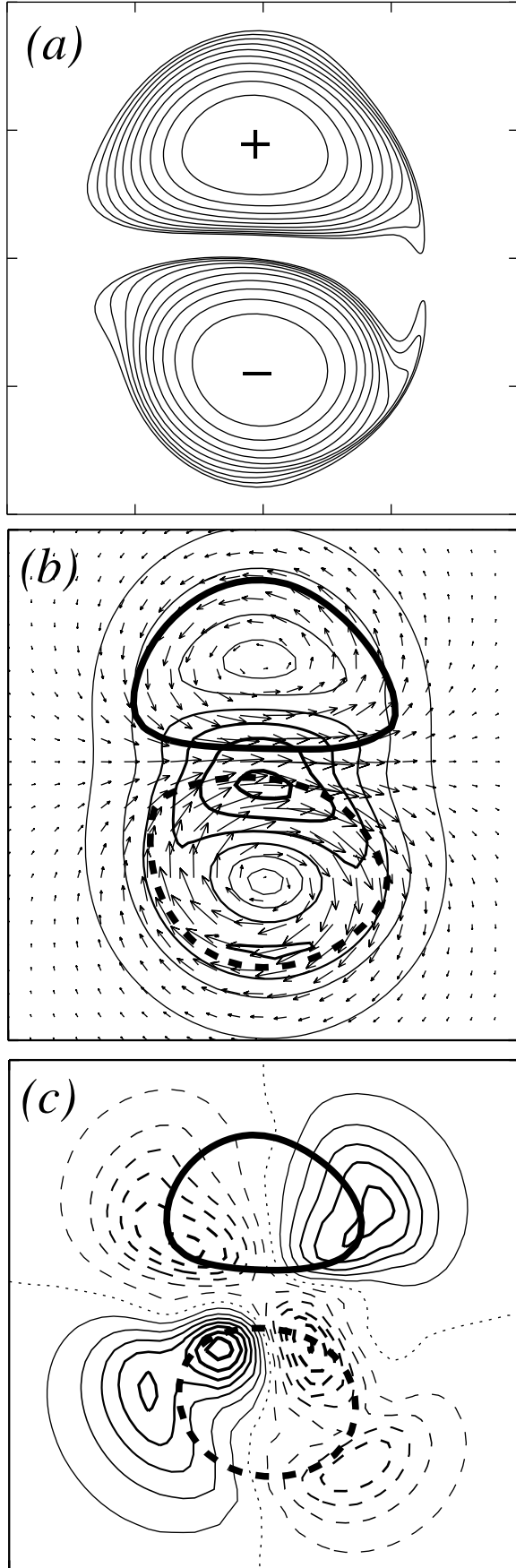


Figure 13. Distributions of w ($w \in [-6.8, 8.5] \times 10^{-2}$, $\delta w = 0.13$) at $t = 26.8T_{bp}$ (a) in the x - y plane at $i_z = 65$ ($z = 0$) and (b) in the x - z plane at $i_y = 65$ ($y = 0$). PV contours $\varpi = -0.2$ at (Figure 13a) $z = 0$ and (Figure 13b) $y = 0$ are shown (dashed thick line). Domain extent is $x, y \in [-\pi, \pi]c$, and $z \in [-\pi, 0]$.



($z = -2.21$, Figure 17). The three-dimensional structure of the *total* w is the result of a wave-wave interaction that lies beyond the scope of this work, it is left for future research.

[42] The total energy $E_T(\mathbf{x}, t)$ is decomposed as

$$E_T = E_{Tb} + E_{Ti} + E_{Tint}, \tag{14}$$

where $E_{Tb} \equiv \mathbf{u}_b^2 + N^2 \mathcal{D}_b^2$, $E_{Ti} \equiv \mathbf{u}_i^2 + N^2 \mathcal{D}_i^2$, and $E_{Tint} \equiv \mathbf{u}_b \cdot \mathbf{u}_i + N^2 \mathcal{D}_b \mathcal{D}_i$ are the total energies of the balanced flow, unbalanced flow, and interaction, respectively. E_{Ti} is one order of magnitude greater than E_{Tb} and E_{Tint} because IGWs are ubiquitous on the domain. Therefore, E_T correlates well with E_{Ti} (Figure 18). The decrease of the spatial average $\langle E_T \rangle(t)$ is about two orders of magnitude smaller than the time mean $\overline{\langle E_T \rangle}$ and is due to the small numerical dissipation.

[43] We note that the unbalanced flow has a small amount of PV (Figure 16c). This *unbalanced* PV, defined as usual from (4) using \mathbf{u}_i and \mathcal{D}_i , may be used to quantify the interaction between the balanced and unbalanced flows. The unbalanced flow φ_i , obtained diagnostically from the *total* flow every time t , is not a *true* flow in the sense that \mathbf{u}_i and \mathcal{D}_i do not necessarily have to fulfill the dynamical equations (A4)–(A7). Therefore the unbalance pair (\mathbf{u}_i and \mathcal{D}_i) may have a nonzero PV (which is a nonlinear quantity). The problem arising from the conservation or nonconservation of PV in the unbalanced flow is a fictitious one, since the unbalanced and balanced flows, separately, do not generally satisfy the dynamical equations.

5.3. Dipole and Gravity Waves Interaction

[44] We analyze here the interaction between a baroclinic dipole identical to case C5 (section 5.1) and a gravity wave with $k = -6/c$ ($\lambda_X/c = 2\pi/(ck) \cong 1$) and $\mathcal{D}_i = 0.2$ (case C7). This implies that the dipole and the wavefield have similar spatial scales and propagate in opposite directions. In this case $\mathcal{D}_i = |\mathcal{D}_b|_{\max} = 0.2$, that is, the PV vertical advection by the wave flow is larger than in the case of a monopolar vortex and a gravity wave discussed in section 4.2.

[45] The large wave motion causes vertical PV vortex advection which largely deforms the PV distribution on horizontal layers (Figures 19a–19c). Since ϖ in the vortices decreases as the distance from the vortex core increases, the vertical advection of PV by the waves is noticeable in Figures 19a–19c as a wave in the PV isolines at $z = 0$ moving westward (the crest is indicated with a solid line in Figures 19a–19c). This PV deformation makes the $|\mathbf{u}_h|$ pattern substantially differ from that typical of a dipole in the absence of gravity waves (Figure 14b). Interestingly, the dipole remains almost unchanged in the isopycnal space, where PV is always conserved, which proves the stability of vortex dipoles under IGWs perturbations (Figure 19d).

[46] To address the Doppler shift frequency in the dipole flow, we improve the numerical resolution by using a dipole

Figure 14. Horizontal distributions at $t = 5T_{ip}$ of (a) PV contours on the middle isopycnal ($z = 0$, PV jump $\delta\varpi = 7.5 \times 10^{-2}$), (b) the horizontal velocity at $i_z = 65$ ($z = 0$, $|\mathbf{u}_h|_{\max} = 0.78$, $\delta|\mathbf{u}_h| = 0.12$, with only every other vector plotted), and (c) the vertical velocity at $i_z = 61$ ($z = -0.15$, $w \in [-7.1, 7.5] \times 10^{-4}$, $\delta w = 10^{-4}$). PV contours $\varpi^\pm = \pm 0.2$ are included in (Figure 14b) and (Figure 14c) at their corresponding depths. Domain extent is $\delta x = \delta y = 2.26c$.

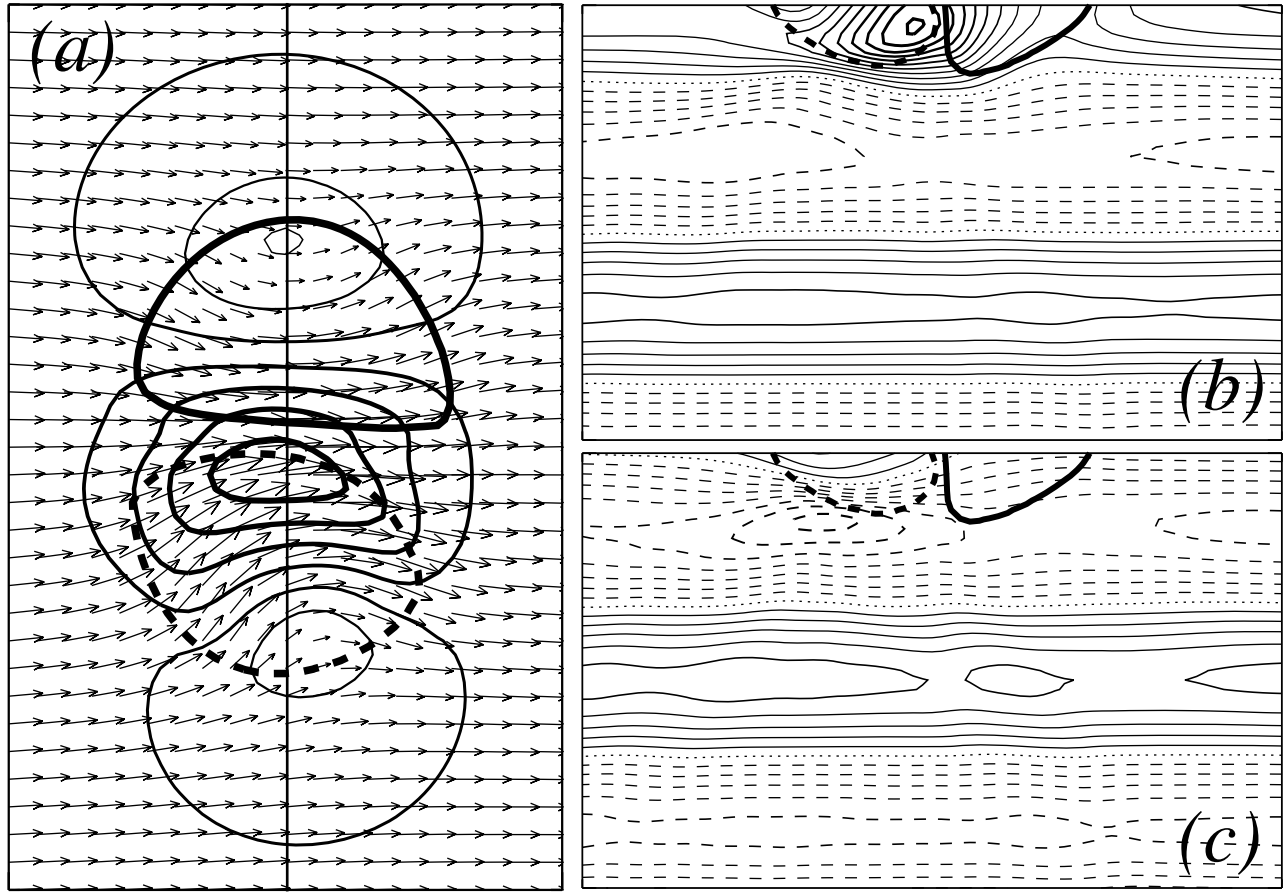


Figure 15. (a) Horizontal distributions of \mathbf{u}_h and $|\mathbf{u}_h|$ at $i_Z = 65$ ($z = 0$, $|\mathbf{u}_h|_{\max} = 1.5$, $\delta|\mathbf{u}_h| = 0.17$). The PV contours $\varpi^\pm = \pm 0.2$ are included. Domain extent is $[\delta x, \delta y] = [2, \pi]c$. Vertical distribution in the y - z plane at $i_X = 27$ ($x = 1.82$) of (b) u ($u \in [-0.85, 1.59]$, $\delta u = 0.14$) and (c) v ($v \in [-1.06, 0.79]$, $\delta v = 0.14$). Domain extent is $y \in [-1.91, 1.91]c$, $z \in [-2.25, 0]$. Time $t = 5T_{ip}$. PV contours $\varpi^\pm = \pm 0.1$ are included for reference. The aspect ratio $L_X/L_Z = L_Y/L_Z = c$ is preserved in Figures 15a–15c.

with semiaxes twice those given above, that is, $a_X^\pm = 1.2c$, $a_Y^\pm = 0.8c$, $a_Z^+ = 0.8$, and $a_Z^- = 0.54$. Three cases of plane gravity waves with $\mathcal{D}_i = 0.01$ are considered, namely, $(k, l) = (8/c, 0)$, $(k, l) = (-8/c, 0)$, and $(k, l) = (0, 8/c)$. Owing to the fact that w_i is three orders of magnitude larger than w_b , the vortical w_b quadrupolar pattern is barely noticeable. Thus, the *total* w pattern closely corresponds to the w_i pattern. In all cases the deformation of the wave phase lines evolves into cyclonic or anticyclonic patterns whether a cyclone or an anticyclone, respectively, is involved (see Figure 20). This is consistent with the monopolar vortex case explained in section 4.2.

[47] However, some differences can be appreciated when a dipole is considered. In the first case (C8, $(k, l) = (8/c, 0)$), u_b is the velocity component relevant in the Doppler shift relation (13) along the dipole axis. After an unsteady regime, k remains approximately stationary relative to the dipole reference frame (though the wave phase θ continues moving eastward), and therefore the x derivative of (13) implies that

$$\frac{\partial k}{\partial x} = -\frac{k}{u_b - U_d} \frac{\partial u_b}{\partial x} \cong -\frac{k}{u_b} \frac{\partial u_b}{\partial x}, \quad (15)$$

where $U_d = 0.02 \ll u_{b \max}$ is the x component of the horizontal dipole velocity. Thus, according to (15), the wavelength λ_X increases (decreases) at the entrance (exit) of the dipole axis, where $\partial u_b / \partial x > 0$ ($\partial u_b / \partial x < 0$), as observed in Figure 20a. In the second case (case C9, $k = -8/c$ and $l = 0$), the wave phase line pattern does not differ significantly from that in the first case (Figure 20a) and is not shown. In the last case (case C10, $k = 0$ and $l = 8/c$), the relevant velocity component in the Doppler shift is v_b . According to (13) ω_j increases where $v_b > 0$ (northeastern and southwestern regions) and decreases where $v_b < 0$ (southeastern and northwestern regions) as can be inferred from Figure 20b.

6. Concluding Remarks

[48] In this work we have numerically investigated the interaction between idealized baroclinic vortical structures and pre-existent plane inertia-gravity waves with similar horizontal velocity or isopycnal vertical displacement amplitudes at the submesoscale. There is a large number of different possible interactions depending on the initial parameters of the vortical structures and IGWs, and we have not attempted

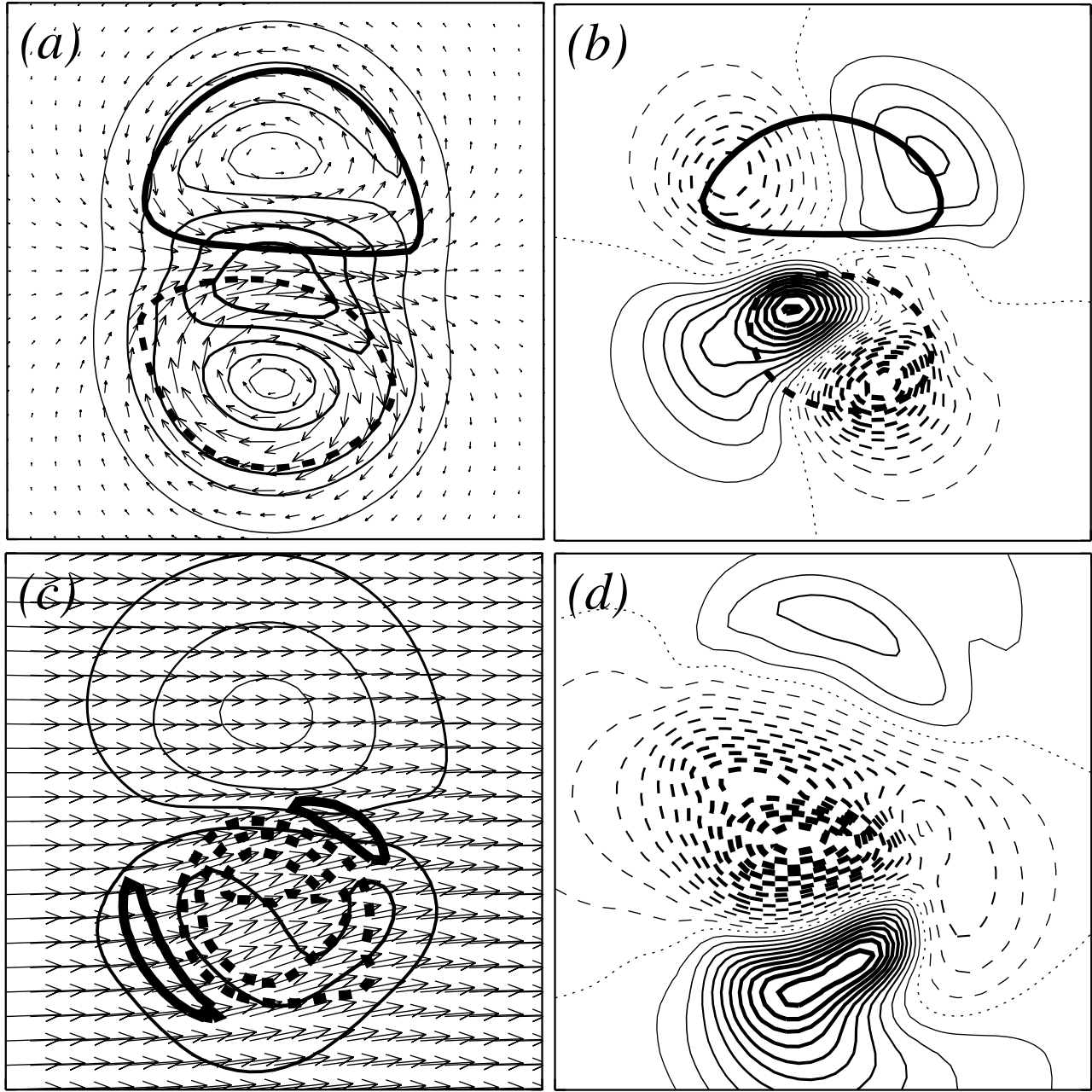


Figure 16. Horizontal distributions at $t = 5T_{ip}$ of (a) \mathbf{u}_{bh} and $|\mathbf{u}_{bh}|$ ($|\mathbf{u}_{bh}|_{\max} = 0.76$, $\delta|\mathbf{u}_{bh}| = 0.12$, $\varpi^{\pm} = \pm 0.2$), (b) w_b ($w_b \in [-17, 16] \times 10^{-4}$, $\delta w_b = 1.4 \times 10^{-4}$, $\varpi^{\pm} = \pm 0.2$), (c) \mathbf{u}_{ih} and $|\mathbf{u}_{ih}|$ ($|\mathbf{u}_{ih}|_{\max} = 0.84$, $\delta|\mathbf{u}_{ih}| = 6.2 \times 10^{-2}$, $\varpi = [-9, 3] \times 10^{-2}$, PV jump $\delta\varpi \cong \pm 0.03$), and (d) w_i ($w_i \in [-32, 21] \times 10^{-3}$, $\delta w_i = 2 \times 10^{-3}$). Figures 16a and 16c are represented at $i_z = 65$ ($z = 0$), and Figures 16b and 16d at $i_z = 61$ ($z = -0.15$), where there is a maxima of total vertical velocity. Domain extent is $\delta x = \delta y = 2.26c$.

to exhaust the very large parameter space. Two main mechanisms are usually involved in this vortex-wave interaction. The first mechanism is the advection of PV by the waves, which makes the vortical structure unsteady and forces it to be permanently in a state of geostrophic adjustment, at the same time that it modifies the upper and lower limits of the IGW frequency wave band. The second mechanism is the advection of waves by the vortices, which changes the local wave frequency through the Doppler shift frequency relation. These mechanisms operate on submesoscale vortical structures with Rossby numbers close to,

but smaller than 1, which remain always stable despite the large amplitude waves.

[49] A remarkable result is the enhancement of the *total* vertical velocity by an order of magnitude when inertial waves are present in vortical flows. This is a clear example of a nonlinear vortex-wave interaction, which results in the generation of right-handed helical waves. Therefore, the wave frequency ranges at initial times from the Coriolis frequency f to an effective frequency f_e and afterward reaches also superinertial frequencies due to resonance mechanisms.

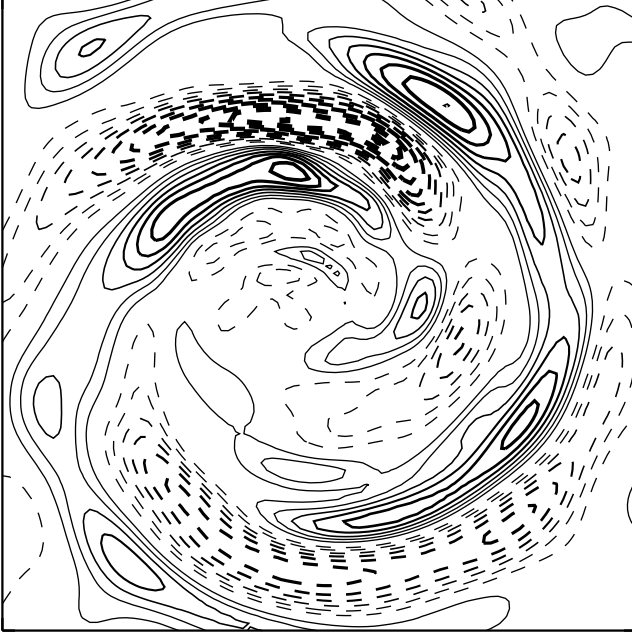


Figure 17. Horizontal distribution of w_i at $i_z = 20$ ($z = -2.21$) and $t = 5T_{ip}$ ($w_i \in [-44, 32] \times 10^{-3}$, $\delta w_i = 4 \times 10^{-4}$). Domain extent is $\delta x = \delta y = 4.32c$.

[50] Finally, we have considered only interactions between two kinds of submesoscale vortical structures (monopolar and dipole vortices) and two kinds of plane waves (inertial and gravity waves), with many other interactions remaining unexplored. Some examples are the interaction between *localized* wave packets of IGWs and submesoscale vortical structures, and the long-term vortex instability of these vortical flows in presence of an inertia-gravity wavefield. We also leave for further research the catalytic behavior of vortical structures triggering IGWs.

Appendix A: Theoretical Basis of the Numerical Model

[51] We consider the isochoric (volume-preserving) motion of a stable stratified fluid in a reference frame rotating with constant angular velocity $f/2$ around the vertical z -axis with respect to an inertial frame. The density anomaly ρ' is defined as

$$\rho'(\mathbf{x}, t) \equiv \rho(\mathbf{x}, t) - \varrho_z z - \rho_0, \quad (\text{A1})$$

where ρ is the mass density, and $\rho_0 > 0$ and $\varrho_z < 0$ are density and density stratification constants. We introduce the pressure anomaly p' as the pressure p (including the centripetal potential) minus the hydrostatic pressure due to a constant vertical density stratification

$$p'(\mathbf{x}, t) \equiv p(\mathbf{x}, t) + g \left(\rho_0 + \frac{1}{2} \varrho_z z \right), \quad (\text{A2})$$

where g is the acceleration due to gravity. The Boussinesq approximation in the vertical component of the momentum equation is

$$-\frac{1}{\rho} \left(\frac{\partial p}{\partial z} + g\rho \right) \cong -\alpha_0 \left(\frac{\partial p}{\partial z} + g\rho \right) = -\alpha_0 \frac{\partial p'}{\partial z} - \alpha_0 g\rho', \quad (\text{A3})$$

where $\alpha_0 \equiv \rho_0^{-1}$ is a constant specific volume. Vector components here always refer to Cartesian components. The basic equations are the nonhydrostatic, balance of linear momentum in a rotating frame under the f plane and Boussinesq approximations, the mass conservation equation, and the isochoric condition,

$$\frac{d\mathbf{u}_h}{dt} + f\mathbf{k} \times \mathbf{u}_h = -\alpha_0 \nabla_h p', \quad (\text{A4})$$

$$\frac{dw}{dt} = -\alpha_0 \frac{\partial p'}{\partial z} - \alpha_0 g\rho', \quad (\text{A5})$$

$$\frac{d\rho}{dt} + \rho \nabla \cdot \mathbf{u} = 0, \quad (\text{A6})$$

$$\nabla \cdot \mathbf{u} = 0. \quad (\text{A7})$$

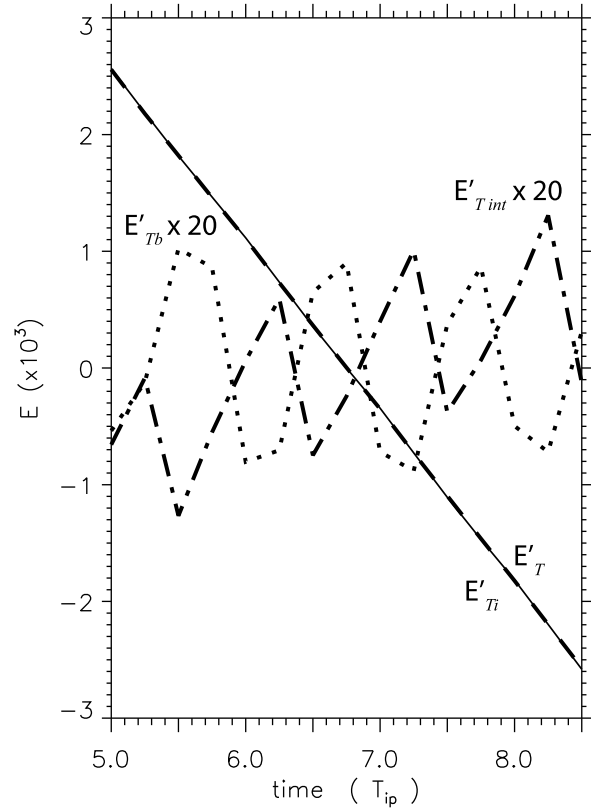


Figure 18. Time evolution of anomalies of the total energy E'_T , total energy of the balanced flow E'_{Tb} , total energy of the unbalanced flow E'_{Ti} , and the total energy of the interaction term E'_{Tint} . Anomalies are defined as $E'_\chi \equiv \langle E_\chi \rangle - \langle E_\chi \rangle$, where $\langle E_\chi \rangle$ is the time average of the spatial three-dimensional domain average $\langle E_\chi \rangle$. The time averages and the standard deviations are $\langle E_T \rangle = 0.55 \pm 0.16 \times 10^{-2}$, $\langle E_{Tb} \rangle = (9.2 \pm 0.37) \times 10^{-4}$, $\langle E_{Ti} \rangle = 0.55 \pm 0.16 \times 10^{-2}$, and $\langle E_{Tint} \rangle = (2.8 \pm 0.35) \times 10^{-4}$. Decreases of E'_T and E'_{Ti} are due to numerical diffusion.

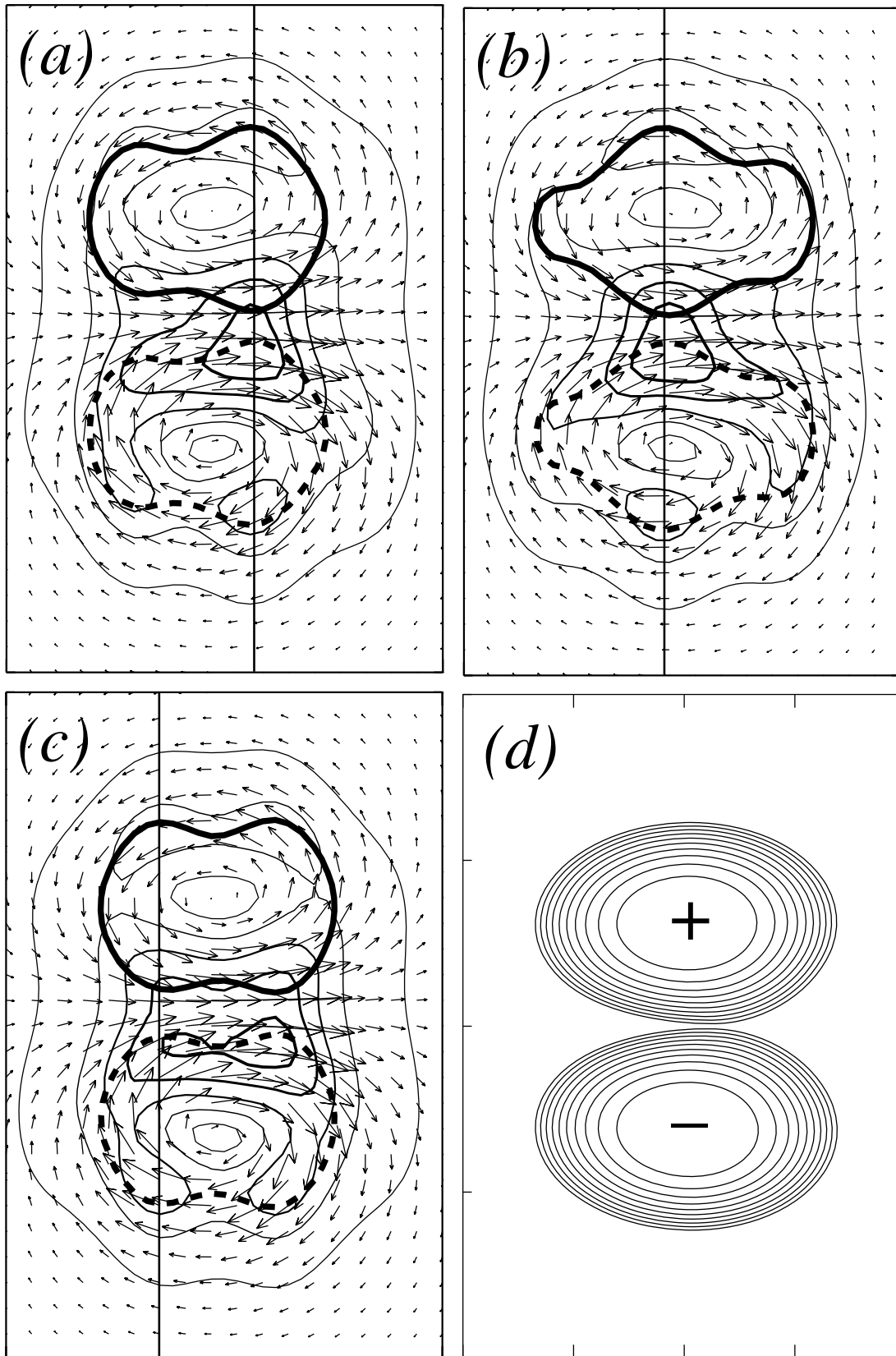


Figure 19. Horizontal distributions of \mathbf{u}_h and $|\mathbf{u}_h|$ ($|\mathbf{u}_h|_{\max} = 0.75$, $\delta|\mathbf{u}_h| = 0.125$) at $i_z = 65$ ($z = 0$) at (a) $t = 2T_{bp}$, (b) $t = 2.2T_{bp}$, and (c) $t = 2.4T_{bp}$. PV contours with $\varpi = \pm 0.2$ are included. Straight solid lines indicate the wave crest position. (d) PV contours on the middle isopycnal ($i_l = 65$, PV jump $\delta\varpi = 7.5 \times 10^{-2}$) at $t = 2.4T_{bp}$. Domain extent is $[\delta x, \delta y] = [1.77, 2.65]c$.

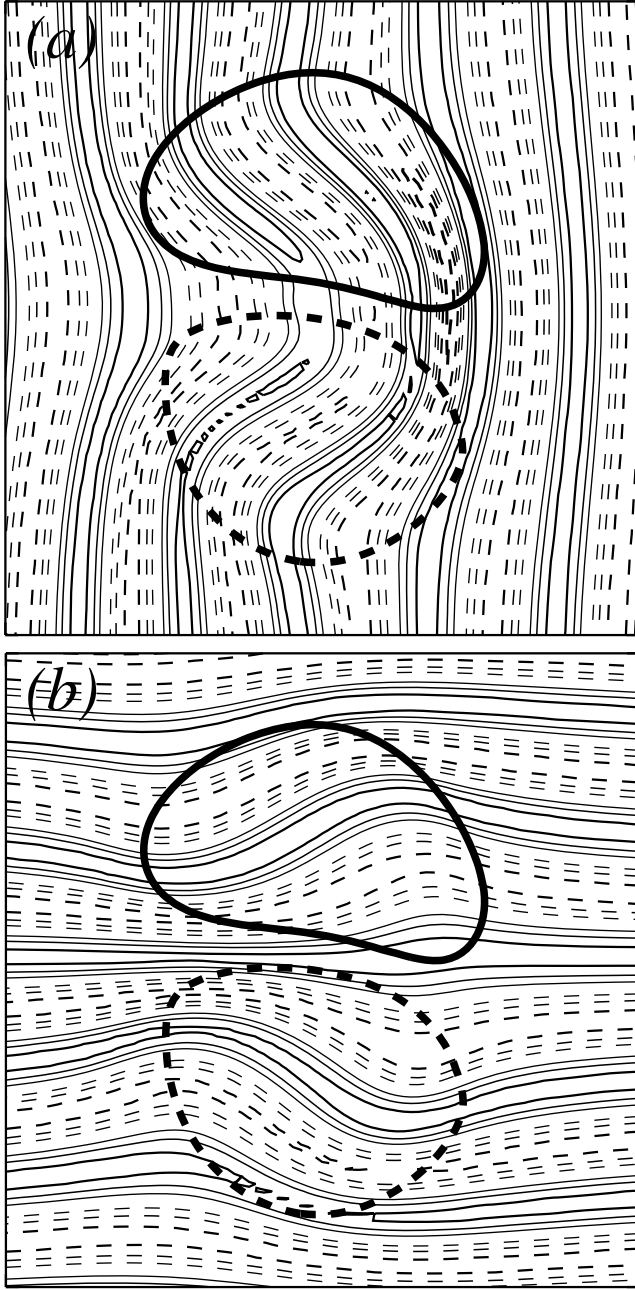


Figure 20. Horizontal distributions of w at $i_z = 65$ ($z = 0$) and at $t = 2.08T_{ip}$ with different wave numbers, (a) $(k, l) = (8/c, 0)$ ($w \in [-8.2, 7.3] \times 10^{-2}$, $\delta w = 18 \times 10^{-2}$) and (b) $(k, l) = (0, 8/c)$ ($w \in [-7.5, 7.5] \times 10^{-2}$, $\delta w = 18 \times 10^{-2}$). Domain extent is $\delta x = \delta y = 4.32c$.

The initial unknowns are the three-dimensional velocity field $\mathbf{u} = (u, v, w)$, the pressure anomaly p' , and the density anomaly ρ' .

[52] The incompressibility condition $d\rho/dt = d(d)/dt = 0$ is expressed in terms of \mathcal{D} as

$$\frac{d\mathcal{D}}{dt} = w. \quad (\text{A8})$$

The vertical displacement of isopycnals \mathcal{D} is related to ρ by

$$N^2(\mathcal{D}(\mathbf{x}, t) - z) = g \left(\frac{\rho(\mathbf{x}, t)}{\rho_0} - 1 \right), \quad (\text{A9})$$

where $N^2 \equiv -\alpha_0 g \rho_z$ is the square of the constant background Brunt-Väisälä frequency.

[53] For any quantity χ let $\tilde{\chi} \equiv \chi/f$. The geostrophic velocity shear is defined through the *thermal wind* expression

$$\frac{\partial \tilde{\mathbf{u}}^g}{\partial z} \equiv -c^2 \mathbf{k} \times \nabla_h \mathcal{D} = c^2 \left(\frac{\partial \mathcal{D}}{\partial y}, -\frac{\partial \mathcal{D}}{\partial x} \right), \quad (\text{A10})$$

where $c = \epsilon^{-1} \equiv N/f$. The relative *pseudovorticity* is the vorticity of the horizontal velocity, defined in Cartesian components as

$$\zeta \equiv \nabla \times \mathbf{u}_h = \left(-\frac{\partial v}{\partial z}, \frac{\partial u}{\partial z}, \frac{\partial v}{\partial x} - \frac{\partial u}{\partial y} \right). \quad (\text{A11})$$

[54] The horizontal gradient of \mathcal{D} (times c^2) may be interpreted as the dimensionless horizontal geostrophic pseudovorticity

$$\tilde{\zeta}_h^g = \left(-\frac{\partial \tilde{v}^g}{\partial z}, \frac{\partial \tilde{u}^g}{\partial z} \right) = \tilde{\omega}_h^g = c^2 \nabla_h \mathcal{D}. \quad (\text{A12})$$

Since ζ is solenoidal ($\nabla \cdot \zeta = 0$), the horizontal divergence of $\tilde{\zeta}_h^g$ is equal to (minus) the differential geostrophic vertical vorticity,

$$-\nabla_h \cdot \tilde{\zeta}_h^g = \frac{\partial}{\partial z} \left(\frac{\partial \tilde{v}^g}{\partial x} - \frac{\partial \tilde{u}^g}{\partial y} \right) = \frac{\partial \tilde{\zeta}_z^g}{\partial z} = \tilde{\zeta}_z^g = -c^2 \nabla_h^2 \mathcal{D}. \quad (\text{A13})$$

Using (A8) it follows that the rate of change of $\nabla \mathcal{D}$ is

$$\frac{d}{dt} \nabla \mathcal{D} = \nabla w - \nabla \mathbf{u} \cdot \nabla \mathcal{D}. \quad (\text{A14})$$

The horizontal component of the above equation expresses the rate of change of $\tilde{\zeta}_h^g$. It is used below to obtain the rate of change of the dimensionless horizontal ageostrophic vorticity $\tilde{\omega}_h' \equiv \tilde{\omega}_h - \tilde{\omega}_h^g = \tilde{\omega}_h - c^2 \nabla_h \mathcal{D}$, where the relative vorticity $\omega \equiv \nabla \times \mathbf{u}$.

[55] The vorticity equation consistent with (A7) is

$$\frac{d\tilde{\omega}}{dt} = \tilde{\omega} \cdot \nabla \mathbf{u} + \frac{\partial \mathbf{u}}{\partial z} + f c^2 \mathbf{k} \times \nabla_h \mathcal{D}, \quad (\text{A15})$$

and is used next to express the material rate of change of $\tilde{\omega}_h'$.

[56] The three-dimensional vector potential $\varphi = (\varphi, \psi, \phi)$ and its Laplacian \mathcal{A} is introduced by the definitions

$$\mathcal{A} = (\mathcal{A}, \mathcal{B}, \mathcal{C}) \equiv \nabla^2 \varphi = (\nabla^2 \varphi, \nabla^2 \psi, \nabla^2 \phi) \equiv \tilde{\omega} - c^2 \nabla \mathcal{D}. \quad (\text{A16})$$

From the divergence of (A16), and using the vector identity

$$\nabla^2 \varphi = \nabla(\nabla \cdot \varphi) - \nabla \times \nabla \times \varphi, \quad (\text{A17})$$

we obtain

$$c^2 \mathcal{D} = -\nabla \cdot \varphi, \quad (\text{A18a})$$

$$\tilde{\mathbf{u}} = -\nabla \times \varphi. \quad (\text{A18b})$$

Table A1. List of Symbols

Symbol	Description	Symbol	Description
ρ	mass density	ρ'	density anomaly
ρ_0	constant density	α_0	constant specific volume
p	pressure	p'	pressure anomaly
ρ_z	stratification constant	Ω	angular velocity
$d(\mathbf{x}, t)$	depth in the reference density configuration of isopycnal located at (\mathbf{x}, t)	\mathcal{D}	vertical displacement of isopycnals
f	Coriolis frequency	f_e	effective Coriolis frequency
N	background buoyancy frequency	\mathcal{N}	total buoyancy frequency
c	Prandtl ratio	$\mathbf{K} = (k, l, m)$	wave number vector
ω_l	local wave frequency	ω_p	particle wave frequency
θ	wave phase	λ	wavelength
σ_z	wave phase velocity	$\mathbf{u} = (u, v, w)$	velocity vector
\mathbf{u}^g	geostrophic velocity	w^q	QG vertical velocity
\mathbf{Q}_h^g	geostrophic \mathbf{Q} -vector	U_d	dipole speed
$\omega \equiv \omega_h + \zeta \mathbf{k}$	relative vorticity	ω^g	geostrophic vorticity
ω'	ageostrophic vorticity	ϖ	PV anomaly
Π	total potential vorticity (PV)	$\varphi = (\varphi, \psi, \phi)$	vector potential
$\mathcal{A} = (\mathcal{A}, \mathcal{B}, \mathcal{C})$	$\nabla^2 \varphi$ Laplacian of φ	\mathcal{F}	Froude number
\mathcal{R}	Rossby number	E_T	total energy

Thus, $c^2 \mathcal{D}$ is the *source* of $-\varphi$, and $-\varphi$ is the velocity potential of $\tilde{\mathbf{u}}$. Consequently, $c^2 \mathcal{D}$ may be interpreted as the source of the velocity potential of $\tilde{\mathbf{u}}$. Because of (A12), the *horizontal* vector $\mathcal{A}_h = (\mathcal{A}, \mathcal{B})$ is the dimensionless horizontal ageostrophic vorticity

$$\mathcal{A}_h = \nabla^2 \varphi_h = \tilde{\omega}_h - \tilde{\omega}_h^g = \tilde{\omega}'_h. \quad (\text{A19})$$

Combining (A14) with (A15) the rate of change of \mathcal{A} is

$$\frac{d\mathcal{A}}{dt} = -f \mathbf{k} \times \mathcal{A}_h + (1 - c^2) \nabla w + \tilde{\omega} \cdot \nabla \mathbf{u} + c^2 \nabla \mathbf{u} \cdot \nabla \mathcal{D}. \quad (\text{A20})$$

The horizontal component of (A20) is (2).

[57] The prognostic fields are therefore \mathcal{A}_h and ϖ (which is explicitly conserved). The horizontal potential φ_h is diagnosed solving $\mathcal{A}_h = \nabla^2 \varphi_h$. The vertical potential ϕ is recovered from φ_h and ϖ as follows. The dimensionless potential vorticity (PV) anomaly $\varpi \equiv \Pi - 1$ may be written in terms of φ

$$\varpi = \mathcal{L}_q \{\phi\} + \mathcal{M} \{\varphi\}, \quad (\text{A21})$$

where the linear operator $\mathcal{L}_q = \nabla_h^2 + \epsilon^2 \partial_{zz}$ is the QG Laplacian operator, and

$$\mathcal{M} \{\varphi\} \equiv -(1 - \epsilon^2) \nabla_h \cdot \varphi_{hz} + \epsilon^2 [\nabla^2 \varphi - \nabla(\nabla \cdot \varphi)] \cdot \nabla(\nabla \cdot \varphi). \quad (\text{A22})$$

The PV equation (A21) is inverted [Dritschel and Viúdez, 2003] to obtain the vertical potential ϕ .

[58] The numerical procedure used to solve the nonlinear equation (A21) is based on iteration. We collect the linear, constant-coefficient terms of ϕ on the left-hand side, and consider all remaining terms (computed using a previous guess for ϕ) as a source on the right-hand side. The result is an equation of the form $\mathcal{L}_q \{\phi^{(i+1)}\} = S\{\varphi, \psi, \phi^{(i)}\}$ where the source $S\{\varphi, \psi, \phi^{(i)}\} \equiv \varpi - \mathcal{M}\{\varphi, \psi, \phi^{(i)}\}$. Given $S\{\varphi, \psi, \phi^{(i)}\}$, this equation is inverted in spectral space to find a new approximation $\phi^{(i+1)}$, that is $\phi^{(i+1)} = \mathcal{L}_q^{-1} \{S\{\varphi, \psi, \phi^{(i)}\}\}$. If $\phi^{(i+1)}$

is such that $\max\{|\phi^{(i+1)}(\mathbf{x}_j) - \phi^{(i)}(\mathbf{x}_j)|, j=1 \dots n_x \times n_y \times n_z\} < \epsilon$, where the tolerance $\epsilon = 10^{-9}$, then the new solution $\phi^{(i+1)}$ is accepted. Otherwise, S is recomputed using the new $\phi^{(i+1)}$, the horizontal potentials (φ, ψ) remain unchanged, and the procedure is repeated ($i \rightarrow i+1$). This process converges in a few iterations, as long as the flow is statically and inertially stable.

[59] Finally, the numerical implementation of (A20) requires the addition of a biharmonic hyperdiffusion term on the right-hand side and the use of a spectral filter in the spatial derivatives in order to reduce numerical instabilities raised from discretization and aliasing. The hyperdiffusion term is $\mu \mathcal{L}_q^4 \mathcal{A}_h$, where μ is the constant hyperviscosity coefficient and the operator $\mathcal{L}_q^4 \equiv \nabla_h^4 + \epsilon^4 \partial_{zzzz}$. The spectral filter $F(k) \equiv \exp(-c_0 (k/k_{\max})^{10})$, where k is the wave number and c_0 is chosen so that $F(k_{\max}) = 10^{-14}$ (Table A1).

[60] **Acknowledgments.** Comments from two anonymous reviewers and support from the Spanish Ministerio de Educación (AP2006-04635) are gratefully acknowledged.

References

- Bühler, O., and M. E. McIntyre (2005), Wave capture and wave-vortex duality, *J. Fluid Mech.*, *534*, 67–95.
- Capet, X., J. C. McWilliams, M. J. Molemaker, and A. F. Shchepetkin (2008), Mesoscale to submesoscale transition in the California current system, Part I: Flow structure, eddy flux, and observational tests, *J. Phys. Oceanogr.*, *38*, 29–43.
- Danioux, E., and P. Klein (2008a), Propagation of wind energy into the deep ocean through a fully turbulent mesoscale eddy field, *J. Phys. Oceanogr.*, *38*, 2224–2241.
- Danioux, E., and P. Klein (2008b), A resonance mechanism leading to wind-forced motions with a $2f$ frequency, *J. Phys. Oceanogr.*, *38*, 2322–2329.
- Dritschel, D. G., and A. Viúdez (2003), A balanced approach to modelling rotating stably stratified geophysical flows, *J. Fluid Mech.*, *488*, 123–150.
- Dubosq, S., and A. Viúdez (2007), Three-dimensional mesoscale dipole frontal collisions, *J. Phys. Oceanogr.*, *37*, 2331–2344.
- Garrett, C., and W. Munk (1979), Internal waves in the ocean, *Annu. Rev. Fluid Mech.*, *11*, 339–369.
- Gascard, J.-C., A. J. Watson, M.-J. Messias, K. A. Olsson, T. Johannessen, and K. Simonsen (2002), Long-lived vortices as a mode of deep ventilation in the Greenland Sea, *Nature*, *416*, 525–527, doi:10.1038/416525a.
- Hoskins, B. J., I. Draghici, and H. C. Davies (1978), A new look at the ω -equation, *Q. J. R. Meteorol. Soc.*, *104*, 31–38.
- Kasajima, Y., K. A. Olsson, T. Johannessen, M.-J. Messias, E. Jeansson, R. G. J. Bellerby, and I. Skjelvan (2006), A submesoscale coherent eddy in

- the Greenland Sea in 2003, *J. Geophys. Res.*, *111*, C07013, doi:10.1029/2005JC003130.
- Kunze, E. (1984), Observations of near-inertial waves in a front, *J. Phys. Oceanogr.*, *14*, 566–581.
- Kunze, E. (1985), Near-inertial wave propagation in geostrophic shear, *J. Phys. Oceanogr.*, *15*, 544–565.
- Lévy, M., P. Klein, and A.-M. Treguier (2001), Impact of submesoscale physics on production and subduction of phytoplankton in an oligotrophic regime, *J. Mar. Res.*, *59*, 535–565.
- Mahadevan, A. (2006), Modeling vertical motion at ocean fronts: Are non-hydrostatic effects relevant at submesoscales?, *Ocean Modell.*, *14*, 222–240.
- McWilliams, J. C. (1985), Submesoscale, coherent vortices in the ocean, *Rev. Geophys.*, *23*, 165–182.
- Miropol'skiy, Yu. Z. (2001), *Dynamics of Internal Gravity Waves in the Ocean*, edited and translated from Russian by O. D. Shishkina, 406 pp., Kluwer Academic Publishers, Dordrecht, Netherlands.
- Molemaker, M. J., J. C. McWilliams, and I. Yavneh (2005), Baroclinic instability and loss of balance, *J. Phys. Oceanogr.*, *35*, 1505–1517.
- Mooers, C. N. K. (1975a), Several effects of a baroclinic current on the cross-stream propagation of inertial-internal waves, *Geophys. Fluid Dyn.*, *6*, 245–275.
- Mooers, C. N. K. (1975b), Several effects of baroclinic currents on the three-dimensional propagation of inertial-internal waves, *Geophys. Fluid Dyn.*, *6*, 277–284.
- Niwa, Y., and T. Hibiya (1999), Response of the deep ocean internal wave field to traveling midlatitude storms as observed in long-term current measurements, *J. Geophys. Res.*, *104*, 10981–10989, doi:10.1029/1999JC900046.
- Pallás-Sanz, E., and A. Viúdez (2007), Three-dimensional geostrophic motion in mesoscale vortex dipoles, *J. Phys. Oceanogr.*, *37*, 84–105.
- Pedlosky, J. (2003), *Waves in the Ocean and Atmosphere*, 260 pp., Springer, Berlin.
- Perkins, H. (1976), Observed effect of an eddy on inertial oscillations, *Deep-Sea Res.*, *23*, 1037–1042.
- Rubenstein, D. M., and G. O. Roberts (1986), Scattering of inertial waves by an ocean front, *J. Phys. Oceanogr.*, *16*, 121–131.
- Rudnick, D. L., and J. R. Luyten (1996), Intensive surveys of the Azores Front 1. Tracers and dynamics, *J. Geophys. Res.*, *101*, 923–939, doi:10.1029/95JC02867.
- Shay, L. K., T. M. Cook, and P. E. An (2003), Submesoscale coastal ocean flows detected by very high frequency radar and autonomous underwater vehicles, *J. Atmos. Oceanic Technol.*, *20*, 1583–1599.
- Steffen, E. L., and E. A. D'Asaro (2004), Meso- and submesoscale structure of a convecting field, *J. Phys. Oceanogr.*, *34*, 44–60.
- Testor, P., and J.-C. Gascard (2003), Large-scale spreading of deep waters in the Western Mediterranean Sea by submesoscale coherent eddies, *J. Phys. Oceanogr.*, *33*, 75–87.
- Thomas, L. N., A. Tandon, and A. Mahadevan (2008), Submesoscale processes and dynamics, in *Ocean Modeling in an Eddying Regime*, *Geophys. Monogr. Ser.*, vol. 177, ed. by M. W. Hecht and H. Hasumi, pp. 17–38, AGU, Washington, D. C.
- van Meurs, P. (1998), Interactions between near-inertial mixed layer currents and the mesoscale: The importance of spatial variabilities in the vorticity field, *J. Phys. Oceanogr.*, *28*, 1363–1388.
- Viúdez, A., and D. G. Dritschel (2003), Vertical velocity in mesoscale geophysical flows, *J. Fluid Mech.*, *483*, 199–223.
- Viúdez, A., and D. G. Dritschel (2004), Optimal potential vorticity balance of geophysical flows, *J. Fluid Mech.*, *521*, 343–352.
- Weller, R. A. (1982), The relation of near-inertial motions observed in the mixed layer during the JASIN (1978) experiment to the local wind stress and to quasi-geostrophic flow field, *J. Phys. Oceanogr.*, *12*, 1122–1136.
- Young, W. R., and M. B. Jelloul (1997), Propagation of near-inertial oscillations through a geostrophic flow, *J. Mar. Res.*, *55*, 735–766.

M. Claret and Á. Viúdez, Institut de Ciències del Mar, CSIC, P. Marítim de la Barceloneta, 37–49, ES-08003 Barcelona, Spain. (mclaret@cmima.csic.es; aviudez@cmima.csic.es)